RESEARCH ARTICLE

Large-scale laboratory study of breaking wave hydrodynamics over a fixed bar

Dominic A. van der A[1] [ID], Joep van der Zanden[1,2] [ID], Tom O'Donoghue[1] [ID], David Hurther[3],
Iván Cáceres[4] [ID], Stuart J. McLelland[5] [ID], and Jan S. Ribberink[2]

[1]School of Engineering, University of Aberdeen, Aberdeen, UK, [2]Department of Water Engineering and Management,
University of Twente, Enschede, Netherlands, [3]Laboratoire des Ecoulements Géophysiques et Industriels, CNRS, University
of Grenoble Alpes, Grenoble, France, [4]Laboratori d'Enginyeria Marítima, Universitat Politècnica de Catalunya, Barcelona,
Spain, [5]Department of Geography, Environment and Earth Sciences, University of Hull, Hull, UK

Abstract A large-scale wave flume experiment has been carried out involving a $T = 4$ s regular wave
with $H = 0.85$ m wave height plunging over a fixed barred beach profile. Velocity profiles were measured at
12 locations along the breaker bar using LDA and ADV. A strong undertow is generated reaching
magnitudes of 0.8 m/s on the shoreward side of the breaker bar. A circulation pattern occurs between the
breaking area and the inner surf zone. Time-averaged turbulent kinetic energy (TKE) is largest in the
breaking area on the shoreward side of the bar where the plunging jet penetrates the water column. At this
location, and on the bar crest, TKE generated at the water surface in the breaking process reaches the
bottom boundary layer. In the breaking area, TKE does not reduce to zero within a wave cycle which leads
to a high level of "residual" turbulence and therefore lower temporal variation in TKE compared to previous
studies of breaking waves on plane beach slopes. It is argued that this residual turbulence results from the
breaker bar-trough geometry, which enables larger length scales and time scales of breaking-generated
vortices and which enhances turbulence production within the water column compared to plane beaches.
Transport of TKE is dominated by the undertow-related flux, whereas the wave-related and turbulent fluxes
are approximately an order of magnitude smaller. Turbulence production and dissipation are largest in the
breaker zone and of similar magnitude, but in the shoaling zone and inner surf zone production is
negligible and dissipation dominates.

1. Introduction

Van Rijn et al. [2013] identified the surf zone as an important area where our understanding and predictive
capability of sediment transport remains poor. In particular, suspended sediment dynamics around the
breaker bar in the outer surf zone, near-bed sediment dynamics in the wave boundary layer under breaking
waves, vertical structure of sediment dynamics in the inner surf zone, and coherent flow structures and
intermittent sediment stirring under breaking waves were highlighted as important topics for future
research. Improving this understanding of the sediment dynamics throughout the surf zone requires a
detailed knowledge of the intrawave hydrodynamics and turbulence structure under breaking waves.

Field measurements have provided valuable insights into the effects of wave breaking on hydrodynamics.
In the surf zone, wave energy dissipation and roller formation affect the main terms in the cross-shore
momentum balance, leading to time-averaged velocities that are strongly nonuniform in the cross-shore
direction [*Garcez Faria et al.*, 2000]. Field studies have also revealed that wave breaking is an important
mechanism of turbulence production [*Thornton*, 1979]. A significant part of breaking-induced turbulence is
dissipated above trough level [*Grasso et al.*, 2012], while the remainder spreads through the water column,
leading to increased magnitudes of Reynolds shear stress and turbulent kinetic energy through the com-
plete water column [*Ruessink*, 2010]. Turbulence dissipation rates decrease with distance from the free sur-
face [*George et al.*, 1994; *Feddersen et al.*, 2007], which indicates that wave breaking is the dominant source
of turbulence dissipation [*Grasso et al.*, 2012].

These field studies generally cover a limited number of cross-shore and vertical measurement locations,
and the irregularity and alongshore-nonuniformity of the wave limits detailed investigation of the temporal

and spatial variation in the hydrodynamics. Consequently, much of our existing knowledge on breaking wave hydrodynamics comes from small-scale laboratory experiments, the most detailed of which are conducted in wave flumes involving fixed, nonmobile beach profiles. Fixed profiles avoid practical complications associated with moving bed levels, and allow the use of high-resolution optical and nonintrusive measurement techniques. Numerous small-scale experiments studied plunging or spilling waves over horizontal [*Chang and Liu*, 1999; *Drazen and Melville*, 2009] or plane sloping bed profiles [*Okayasu et al.*, 1986; *Nadaoka et al.*, 1989; *Ting and Kirby*, 1994, 1995, 1996; *Cox and Kobayashi*, 2000; *Govender et al.*, 2002; *Stansby and Feng*, 2005; *De Serio and Mossa*, 2006; *Shin and Cox*, 2006; *Kimmoun and Branger*, 2007; *Huang et al.*, 2009; *Sou et al.*, 2010; *Ting and Nelson*, 2011; *Sumer et al.*, 2013]. *Ting and Kirby's* studies [1994, 1995, 1996] have shown that the production and transport of turbulent kinetic energy (TKE) are different for different breaker types. Plunging breakers lead to an injection of TKE into the water column, which is rapidly advected downward by the plunging jet and large vortices. Turbulence under plunging waves is further characterized by strong dissipation, which leads to a large temporal variation in TKE throughout the wave cycle. Since most transport of TKE takes place rapidly after injection during the wave crest, net transport of TKE is in the onshore direction [*Ting and Kirby*, 1994; *De Serio and Mossa*, 2006]. Under spilling breakers, turbulence is more gradually entrained into the water column by diffusion, and dissipation rates are lower, leading to a fairly constant time-variation in TKE throughout the wave cycle and net transport of TKE in the offshore direction as a result of the undertow. Assuming that suspended sediment transport is linked to the turbulence transport, these two mechanisms may partly explain onshore sandbar migration during calm swell wave conditions (plunging waves) and offshore migration under stormy conditions (spilling waves) [*Ting and Kirby*, 1994].

Although breaking wave characteristics over a barred profile may differ significantly from those on a plane sloping beach [*Smith and Kraus*, 1991], relatively few laboratory studies examined the velocity and turbulence characteristics of waves breaking over a bar. Existing studies which included turbulence measurements under breaking waves over a barred profile have been conducted in small-scale wave flumes with fixed beds [*Boers*, 2005; *Govender et al.*, 2011] and in large-scale wave flumes with fixed [*Scott et al.*, 2005] or mobile beds [*Yoon and Cox*, 2010; *Brinkkemper et al.*, 2016; *van der Zanden et al.*, 2016]. Most of these studies showed a strong cross-shore variation across the bar with TKE being highest on, or slightly shoreward of, the bar crest where the waves are breaking [e.g., *Boers*, 2005; *Scott et al.*, 2005; *Yoon and Cox*, 2010; *van der Zanden et al.*, 2016] and that at these locations breaking-induced TKE may reach the bed [*Scott et al.*, 2005; *van der Zanden et al.*, 2016]. In the bar trough, the TKE profiles showed a local minimum compared to adjacent locations since the TKE is mixed over a greater water depth [*Yoon and Cox*, 2010]. *Boers* [2005] correlated the orbital velocity to the TKE and identified in the vicinity of the breaker bar a phase lag between the production of turbulence near the water surface (during wave crest phase) and the arrival of turbulence at the bed (during wave trough phase). At the other locations in the surf zone the correlation appeared to be minimal. A strong phase coupling between the turbulence and orbital motions under plunging waves was also found in a recent large-scale experiment by *Brinkkemper et al.* [2016]. Their ensemble-averaged results, for three elevations at one surf zone location, reveal highest intrawave TKE at the wave front. They also showed that under their full-scale rippled bed conditions where the boundary layer is turbulent, the bed-generated TKE can have similar magnitude as the TKE closer to the water surface.

While useful insights have been obtained from the breaking wave studies on plane sloping beach profiles it is evident that the flow and turbulence fields under breaking waves on barred profiles are significantly different, yet much less studied. Moreover, most of the existing studies have focussed primarily on the time-averaged flow and turbulence, and not on the detailed intrawave flow and (horizontal and vertical transport of) turbulence around the bar, which ultimately are important to understand the sediment transport dynamics. The aim of the present experiment was therefore to obtain such detailed measurements of the flow and turbulence under a large-scale plunging breaking wave around a fixed breaker bar. The experiment was conducted in the large-scale CIEM wave flume as part of a larger experimental campaign to study hydrodynamics and sediment transport processes under breaking waves. Measurements of near-bed hydrodynamics and turbulence under a breaking wave over a mobile bed, obtained as part of this project, were reported in *van der Zanden et al.* [2016]. The fixed bed experiment described in the present paper involves the same wave condition as in *van der Zanden et al.* [2016]. The experiment distinguishes itself from previous barred profile experiments by the high spatial resolution of the measurements, the use of high-

resolution optical instrumentation (LDA) and a regular wave condition which enables us to get insight into the intrawave velocities and turbulence, while the large-scale of the experiment further ensures that turbulence generated in the boundary layer is representative of field-scale conditions.

Section 2 of the paper describes the experiment and the data processing methods. The results are presented in four sections as follows: water surface elevation results are presented in section 3; intrawave and time-averaged horizontal and vertical velocities are presented in section 4; section 5 presents time-averaged TKE, turbulence intensities and Reynolds shear stress along the profile; section 6 presents an analysis of the TKE transport, production and dissipation across the barred profile, from the shoaling zone through to the inner surf zone. The results are discussed in section 7 and the main conclusions are summarized in section 8.

2. Experiments

2.1. Experimental Facility and Bed Profile

The experiment was conducted in the 100 m long, 3 m wide, and 4.5 m deep wave flume at the Polytechnic University of Catalunya in Barcelona (Figure 1a). The wave generation system consists of a wedge-type wave paddle and the steering signals were based on first-order wave generation. The coordinate system has its x origin at the toe of the wave paddle in its rest position and is positive in the direction of the waves; the vertical z coordinate has its origin at the still water level and is positive upward; the y coordinate has its origin on the right side wall of the flume when facing the beach and is positive toward the center of the flume. Throughout this paper η is the water surface elevation, $\bar{\eta}$ the mean water level (mwl), h the water depth, H the wave height, and subscript p indicating wave height (near the paddle) in the constant depth section of the flume; u, v, and w are velocity components in the x, y, and z directions, respectively.

The beach profile for the fixed bed was created in a preceding experiment [*van der Zanden et al.*, 2016] by running the same regular wave condition as used in the present experiment for 3 h over a mobile sand bed profile (sand grain diameter $d_{50} = 0.25$ mm), which initially consisted of a 1:10 offshore slope raised to 1.35 m above the flume floor, followed by a 18 m long horizontal bed, and terminated by a nonmobile straight sloping beach. The rather long horizontal section was chosen in order to ensure that bed slope effects in the inner surf zone or swash zone processes did not affect the hydrodynamics around the bar. After 3 h of waves a breaker bar was created that was sufficiently high to ensure a strongly plunging wave
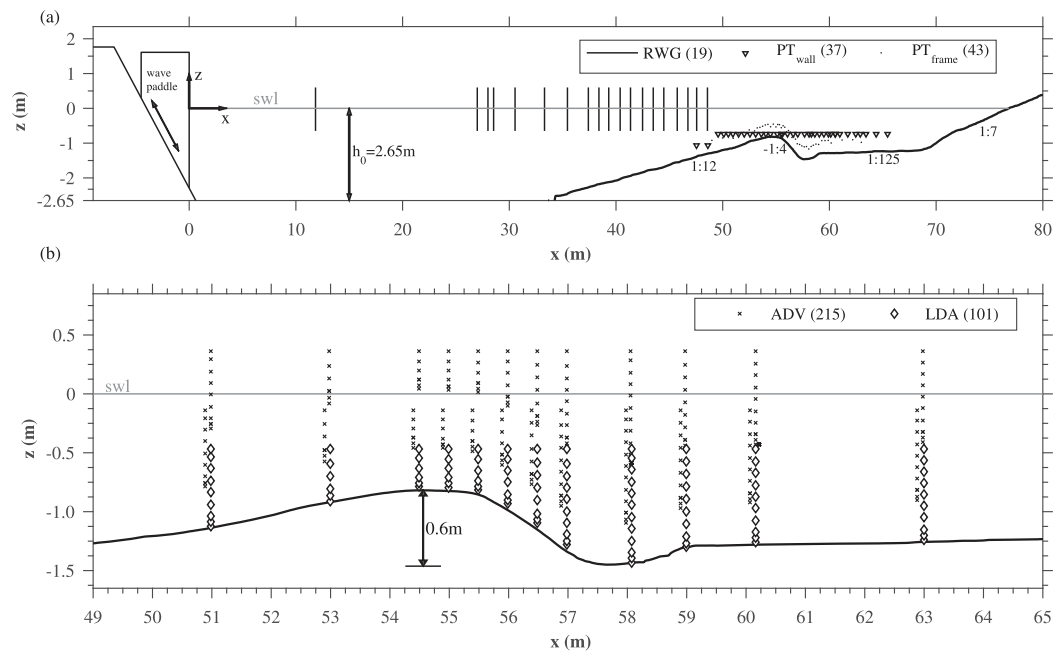

Figure 1. (a) Fixed bed profile and the locations of the resistive wave gauges and pressure transducers; (b) close-up of the velocity measurement area around the breaker bar showing the positions of the ADV and LDA velocity measurements.

with a highly repeatable breaker location. We note that after 3 h the bar had not yet reached a morphodynamic equilibrium, as can be seen in Figure 3 of *Ribberink et al.* [2014]. To construct the fixed bed, the top 10 cm layer of sand was removed from the profile and a 20 cm layer of concrete was added on top, which was allowed to cure for approximately 40 days prior to the start of the experiment. The resulting fixed bed profile consisted of a 1:12 offshore slope, a 0.6 m high breaker bar (measured from crest to trough), with a lee-side slope of approximately 1:4, followed by a 10 m long 1:125 slope and terminated by a fixed 1:7 sloping profile (see Figure 1). The profile corresponds approximately to the bed profile at $t = 60$ min in the accompanying mobile-bed experiment [*van der Zanden et al.*, 2016]. The roughness of the concrete surface was reasonably uniform across the profile and estimated to be of the order of 1–2 mm. On the lee-side of the bar the roughness was approximately twice as large, due to cement leaking away on the steep slope during the curing process, which exposed some of the coarser aggregates at the surface.

2.2. Test Condition

The water depth in the horizontal part of the flume was 2.65 m and the wave condition consisted of a regular wave with wave period $T = 4$ s and a target wave height of $H_p = 0.85$ m at the paddle. The surf similarity parameter is defined as:

$$\xi_0 = \frac{\tan \beta}{\sqrt{H_0/L_0}} \tag{1}$$

where $\tan \beta$ is the 1:12 beach slope, H_0 is the deep water wave height which was obtained from a linear wave shoaling calculation using the wave height in the constant depth section of the flume and the deep water wave length $L_0 = gT^2/2\pi$. $\xi_0 = 0.44$, which is consistent with the plunging breaker realized in the flume and in agreement with *Smith and Kraus's* [1991] classification for barred profiles. More details of the wave breaking characteristics will be presented in section 3. In each "run" waves were generated for a duration of 38 min.

2.3. Measurements

Water surface elevations were measured with sidewall-mounted resistive wave gauges at 19 locations along the flume, from $x = 12$ m in the constant depth section of the flume to $x = 49$ m in the shoaling zone (Figure 1a). Resistive wave gauges were not deployed in the surf zone since they suffered from spurious measurements due to the strong splash-up of water. For the remainder of the profile, pressure transducers (STS-ATM/N) were therefore fitted along the flume sidewall at approximately 0.5 m x spacing. Water surface elevations were retrieved from the pressure measurements after correcting for pressure attenuation due to depth using linear wave theory. Comparison of water surface elevation measured by collocated pressure sensors and resistive wave gauges at two locations in the prebreaking area showed good agreement, with maximum difference of approximately 10%. The resistive wave gauges and pressure transducers were sampled at 40 Hz.
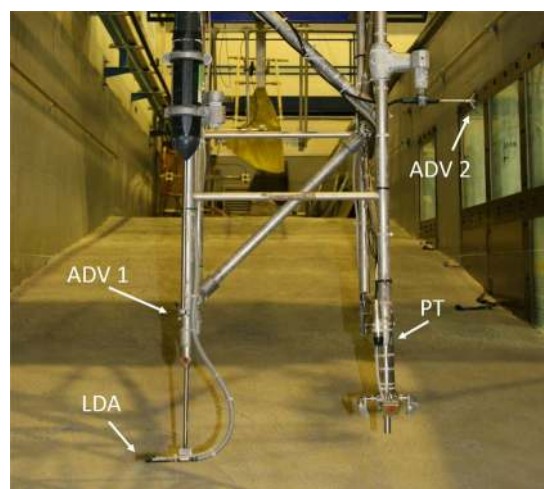
Velocities were measured at 12 cross-shore locations along the bar region (Figure 1b) using a Laser Doppler Anemometer (LDA) and two Acoustic Doppler Velocimeters (ADV) deployed from a measurement frame attached to a carriage on top of the flume (Figure 2). This "mobile frame" allowed the instruments to be positioned at any cross-shore location with 1 cm accuracy and in the vertical with 1 mm accuracy [for more details on the frame, see *Ribberink et al.*, 2014]. The two-component backscatter LDA system consisted of a 14 mm diameter submersible transducer probe with 50 mm focal length powered by a 300 mW Ar-Ion air-cooled laser. The LDA measured the u and w velocity components in an ellipsoidal shaped measurement volume of

Figure 2. Mobile measurement frame indicating the instrumentation positions Note that the instrument on the bottom right (3C-Acoustic Doppler Velocity Profiler) was not used for the present study.

115 μm maximum diameter and approximately 2 mm length in the y direction. For given seeding particle density, the sampling frequency of the LDA depends on velocity magnitude and, therefore, varies throughout the wave cycle. Data rates for the present experiment typically varied between 100 and 600 Hz.

Three-component velocity measurements were obtained from the ADVs (Nortek Vectrino), one of which was positioned on the same side of the frame as the LDA, while the other (ADV2) was positioned on the other side of the frame (Figure 2). The size of the cylindrical shaped measurement volume of both ADVs was 6 mm in diameter and 2.8 mm in length in the y direction. The vertical spacing between the LDA and ADV1 was 0.33 m and between the LDA and ADV2 was 0.83 m. The ADV sampling frequency was 100 Hz. The mobile frame also contained a pressure transducer (PT$_{frame}$) to measure water surface elevation at the frame measurement location (Figure 2a).

The mobile frame could be vertically repositioned during a wave run, allowing typically three vertical measurement positions to be covered during one wave run. At each cross-shore measurement position, LDA velocities were measured at 1, 5, and 10 cm above the bed, and at 10 cm vertical increments higher up, until the limit of the frame's vertical movement was reached, which corresponds to the LDA reaching $z = -0.47$ m. The lowest measurements for ADV1 and ADV2 were at 34 cm and 84 cm above the bed, respectively, and the remaining ADV measurement elevations followed the same incremental changes as the LDA, reaching maximum elevations of $z = -0.13$ m and $z = 0.37$ m for ADV1 and ADV2, respectively.

2.4. Data Processing

For each 38 min run (=570 waves), the first 400 s (=100 waves) of data were discarded because the hydrodynamics were still developing in the flume, which could be visually observed by a gradual change in the wave breaking location. After 400 s the breaking location and breaking wave characteristics were stable, indicating that the hydrodynamics in the breaking zone had reached a quasi-equilibrium state. The remainder of the time series was used to obtain ensemble-averaged quantities. All water surface and velocity data were high-pass filtered with a cutoff frequency of 0.125 Hz (=$0.5/T$) in order to remove the low frequency ($f = 0.022$ Hz) standing wave in the flume which had an amplitude of a few cm.

Data from the resistive wave gauges and the sidewall-mounted pressure transducers were averaged over multiple runs since these instruments had fixed x locations. During a full 38 min run, the mobile frame measurement frame covered three vertical elevations for a duration of 10 min each, which is equivalent to 150 waves for each (x, z)-velocity measurement. A total of 150 waves for ensemble-averaging were similar to *Scott et al.* [2005], and more than *Ting and Kirby* [1994] and *Shin and Cox* [2006], who used 100 waves.

Spikes in the ADV velocity data occurred as a result of air bubbles entrained by the wave breaking process. This particularly happened at instances of intense plunging above the downward slope of the bar and in the upper part of the water column throughout the inner surf zone. A combination of approaches was used to despike the ADV velocity data. First the 3-D phase-space method of *Mori et al.* [2007] was applied to remove spikes in the time series. Then, any data having correlation values below 80% and Signal-to-Noise-Ratio (SNR) below 15 dB were identified as poor quality data in the time series. Finally, at the ensemble-averaging stage, any data at a given wave phase that deviated by more than four standard deviations from the median value at that phase was also considered an outlier. Poor quality of spurious velocity data identified during the last two steps was removed from the analysis of the data set. The proportion of data removed depends strongly on the cross-shore location of the measurement and the phase of the wave, and their occurrence in the time series could therefore vary between a few percent in the prebreaking area to 100% during certain phases at locations where the plunging jet penetrates the water column and air bubbles lead to significant attenuation of the acoustic signal. Phase-averaged velocities based on <15 wave cycles, and turbulence results based on <40 wave cycles [*Shin and Cox*, 2006], were therefore excluded from the results, which explains why there are "gaps" in the results presented later and why at most locations results are only shown below the wave trough level.

The LDA data suffered from fewer poor quality measurements because the data are SNR-validated instantaneously during acquisition, and, when a bubble traverses through the measurement volume or laser beam paths the LDA records nothing rather than recording an erroneous measurement. Moreover, the LDA measurement volume and the laser beams are significantly smaller than the ADV measurement volume and the acoustic beams, which means there is less chance of a bubble obstructing the LDA measurement. The LDA

data were therefore despiked using the median filter only, and, similar to the ADV, only phases for which there were >15 or >40 data points for velocities and turbulence results, respectively, were retained.

Since not every generated wave is exactly equal in period to the target of $T = 4.00$ s, we applied conditional averaging following the method of *Petti and Longo* [2001]. Applied to water surface elevation η, the averaging of N waves is given by:

$$\langle \eta(t) \rangle = \frac{1}{N} \sum_{n=0}^{n=N-1} \eta(t + t_n) \qquad 0 \leq t < T_{med} \tag{2}$$

where t_n is the cyclic trigger, defined as the time instant of the nth wave zero up-crossing measured by the resistive wave gauge at $x = 35.4$ m. *Petti and Longo* [2001] restricted the time-interval to $0 \leq t < \min(T)$ and subsequently stretched the data linearly to cover the mean wave period. Here we restricted data to $0 \leq t < T_{med}$, with T_{med} being the median wave period, which for every run was equal to the target period of $T = 4.00$ s. All water surface, pressure, and velocity measurements were ensemble-averaged following equation (2). Note that due to the irregular sampling of the LDA data the averaging process is slightly different to the ADV data: instead of averaging all the data at the same phase instant, we average all data falling within an interval of 0.01 s centred on the phase instant (equivalent to 100 Hz sampling rate similar to the ADV sampling rate).

After ensemble-averaging the instantaneous horizontal velocity u can be decomposed as follows:

$$u = \overline{u} + \tilde{u} + u' \tag{3}$$

where $\overline{u}$ is the time-averaged velocity, $\tilde{u}$ is the wave-related component, and u' is the turbulent fluctuation; $\langle u \rangle = \overline{u} + \tilde{u}$ is the ensemble-averaged component. The instantaneous vertical and transverse velocity components are decomposed in a similar manner to equation (3).

3. Water Surface Elevation

Figure 3 shows the wave height, the root-mean-square water surface elevation, η_{rms}, and mean water level, $\overline{\eta}$, along the flume. The wave starts to overturn at $x = 52$ m and the plunging wave jet hits the water surface on top of the bar at $x = 54.5$ m. The penetration of the jet into the water column pushes up a body of water that subsequently strikes the surface at 58–59 m. Following *Smith and Kraus* [1991], we refer to these locations as the break point, the plunge point, and the splash point, respectively. To be consistent with *van der*
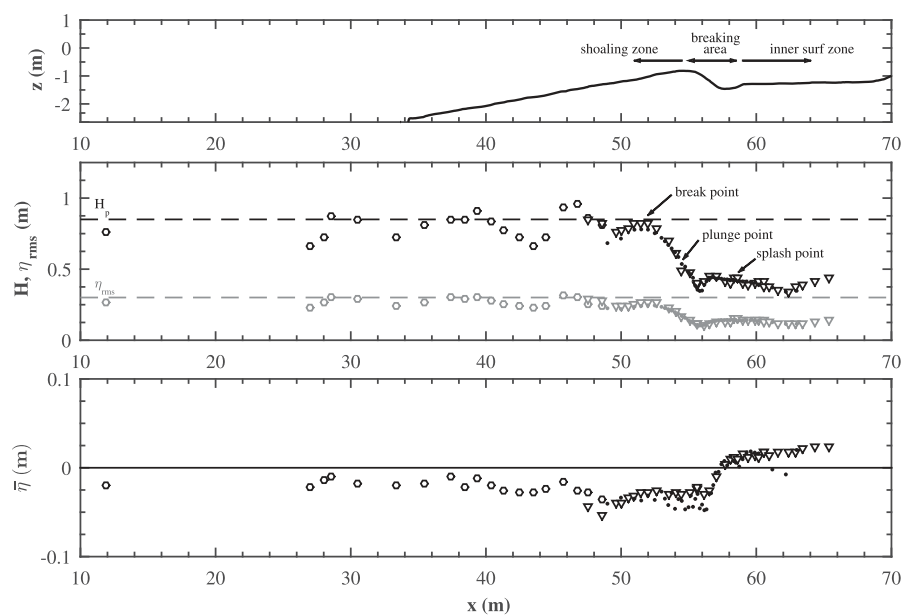

Figure 3. (top) Bed profile; (middle) wave height (black) and root-mean-square water surface elevation (gray); (bottom) wave set up. Open circles: resistive wave gauges; triangles: pressure sensors along flume sidewall; dots: mobile frame pressure sensor.

Table 1. Wave Characteristics at the 12 Velocity Measurement Locations: Water Depth h, Wave Height H, Set Up $\bar{\eta}$; L Is the Wave Length Obtained From Linear Wave Theory and $(gh)^{0.5}$ Is Shallow Water Wave Speed

x (m)	h (m)	H (m)	$\bar{\eta}$ (cm)	L (m)	$(gh)^{0.5}$ (m/s)	h/L	H/h
51.0	1.10	0.78	−3.5	12.5	3.3	0.09	0.71
53.0	0.89	0.72	−2.7	11.4	3.0	0.08	0.81
54.5	0.78	0.54	−3.7	10.7	2.8	0.07	0.69
55.0	0.78	0.48	−4.4	10.7	2.8	0.07	0.62
55.5	0.82	0.38	−3.5	11.0	2.8	0.07	0.47
56.0	0.94	0.35	−4.1	11.7	3.0	0.08	0.37
56.5	1.13	0.44	−2.8	12.7	3.3	0.09	0.39
57.0	1.34	0.43	−0.5	13.7	3.6	0.10	0.32
58.0	1.46	0.42	1.2	14.2	3.8	0.10	0.29
59.0	1.32	0.41	1.0	13.6	3.6	0.10	0.31
60.2	1.30	0.39	1.6	13.5	3.6	0.10	0.30
63.0	1.28	0.35	2.0	13.4	3.5	0.10	0.27

Zanden et al. [2016], the breaking region is here defined as the region between the break point and the splash point. The regions offshore and onshore of the breaking area are referred to as the shoaling zone and the inner surf zone, respectively. Figure 3 shows an oscillation in wave height along the offshore bar slope and in the constant depth section of the flume. The oscillation is likely caused by crosswaves and/or free secondary wave effects, both of which are inherent to first-order mechanical generation of energetic regular short waves [*Hughes*, 1993]. Inspection of the time series revealed that the cross-shore variation in H commences with the first waves generated during a run, suggesting that short-wave reflection by the breaker bar or by the end slope is not the primary cause for the oscillations in H. The oscillation along the offshore slope is much smaller in magnitude than the wave height decay in the breaking region, and we assume therefore that these secondary waves are of minor importance for the breaking process and hydrodynamics in the test section.

The mean water level shows a set-down of approximately 2.5 cm until $x = 57$ m followed by a set up of approximately 2.5 cm. The rapid change in mean water level from set-down to set up, and the lag between the breaking point (at $x = 52$ m) and the initiation of set up (at $x = 57.3$ m) were also observed in previous studies involving a barred profile [*Sancho et al.*, 2002; *Boers*, 2005; *Scott et al.*, 2005; *Govender et al.*, 2011]. The lag occurs because the wave energy is not immediately dissipated when the wave tumbles over at the breakpoint $x = 52$ m; instead dissipation into heat takes place shoreward of the plunge point ($x > 55$ m) in the propagating bore [*Svendsen*, 1984; *Battjes*, 1988]. Table 1 presents summary statistics for the measured wave hydrodynamics at the 12 measurement locations.

Figure 4 shows snapshots from a video recording of the breaking process and the corresponding water surface profile along the bar measured by the mobile frame pressure transducer. Note that the left-hand side of the images corresponds to $x = 53$ m while the water surface profiles begin at $x = 50$ m, the top right of the image corresponds to approximately $x = 64$ m. In this figure, and throughout the remainder of the paper, time ($t/T = 0$) is referenced to the moment of wave zero up-crossing at $x = 50$ m (Figure 4a). Figure 4b shows how the plunging jet just hits the undisturbed water surface of the adjacent wave trough. This plunge point happens on the top of the breaker bar at $x \approx 54.5$ m. The curling jet traps a large amount of air, which can be seen under the water surface of the crest in Figure 4c. In this image, the plunging jet is penetrating the water column and pushing up a body of water which forms a new wave, as can be seen from the two crests in the pressure recording. Note that the pressure sensors measure the "green water", i.e., the highly aerated "white water" in between the two crests is not measured by the pressure sensor. Figure 4d shows how the pushed up water body splashes-up at around $x = 59$ m. While the splash-up occurs, the main incoming plunging jet is still penetrating the water column and causing the distinct streak of white water at the water surface. The air entrained during the plunge has in the meantime propagated with the wave in the onshore direction. The splash-up process repeats another time in Figure 4d, although to a lesser extent, after which the wave propagates further as a uniform bore.

The breaking process for a plunging wave, involving jet penetration, push-up, and splashing, has been described in detail previously [e.g., *Peregrine*, 1983] and observed in previous laboratory studies [*Ting and Kirby*, 1995; *Govender et al.*, 2002; *Kimmoun and Branger*, 2007]. The sequence of images shows that the bubble plumes caused by the plunging jet and the subsequent splash-up event remain present during the entire wave cycle, which indicates that high levels of turbulence are present in the flow throughout the entire flow
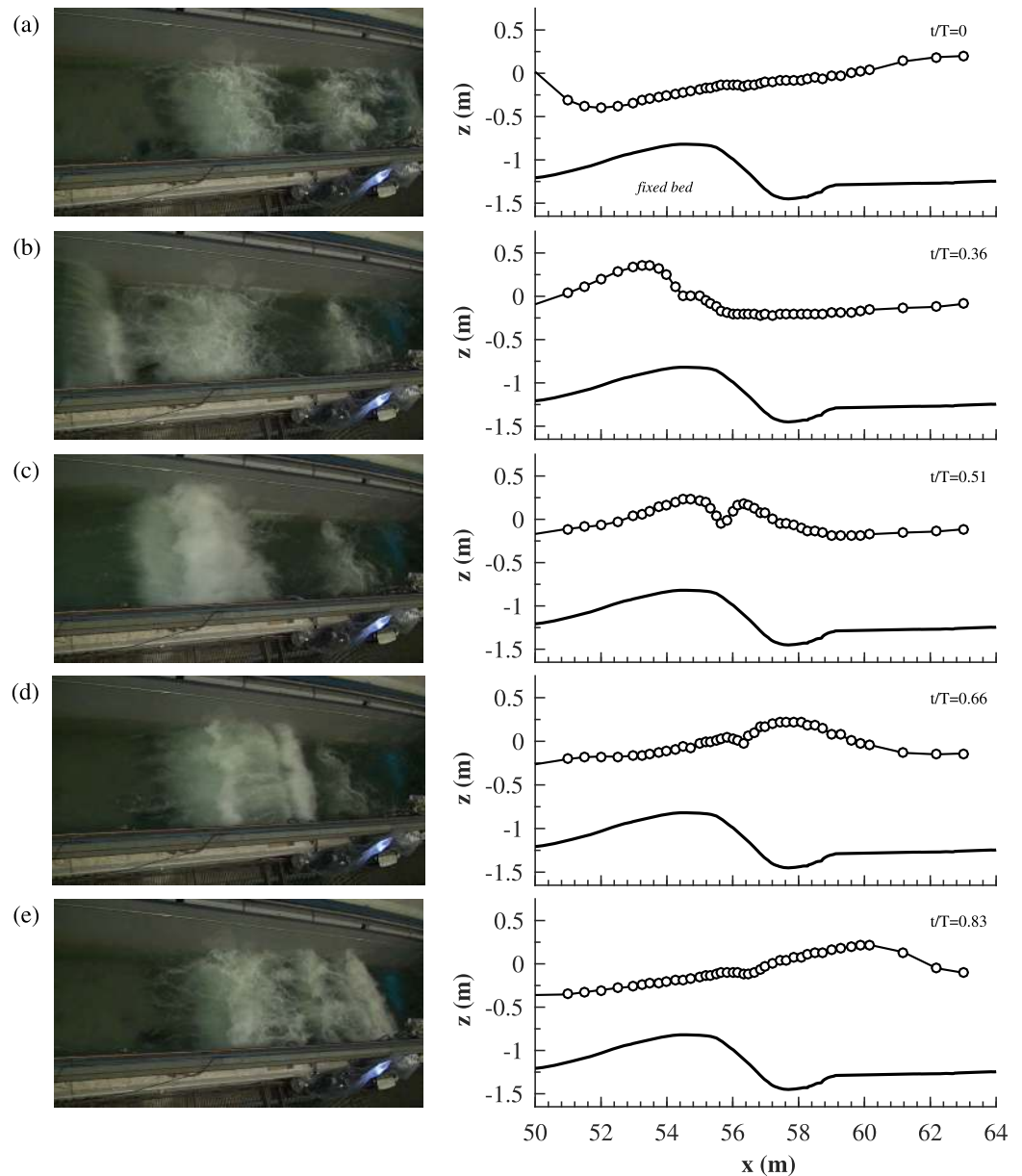
Figure 4. Wave breaking sequence from video frames and corresponding water surface elevations measured by the mobile frame pressure transducer: (a) wave incoming at $x = 50$ m; (b) plunging jet hitting the water surface; (c) air entrainment and push up of water; (d) splash-up; (e) secondary splash-up. The top left of the image is approximately at $x = 53.4$ m. The LDA laser beams located at $x = 63$ m (in this case) can be vaguely seen in the right-hand side of images (a)–(d)

cycle. High levels of turbulence imply strong mixing within the bubble plumes, however the distinct narrow plumes in images (a) and (b) further suggest that no strong horizontal mixing is taking place between the plumes and the surrounding fluid. The plumes are advected shoreward under the wave crest and in the off-shore direction under the wave trough; the latter is best observed by comparing images (a) and (b). This observation suggests strong intrawave advection of turbulence, which will be examined in section 5.

4. Flow Velocities

4.1. Time-Averaged Velocities
Figure 5 shows vertical profiles of the time-averaged horizontal and vertical velocities. The time-average was only taken if valid data existed for at least 90% of the (wetted) flow cycle. Due to the disturbing effect
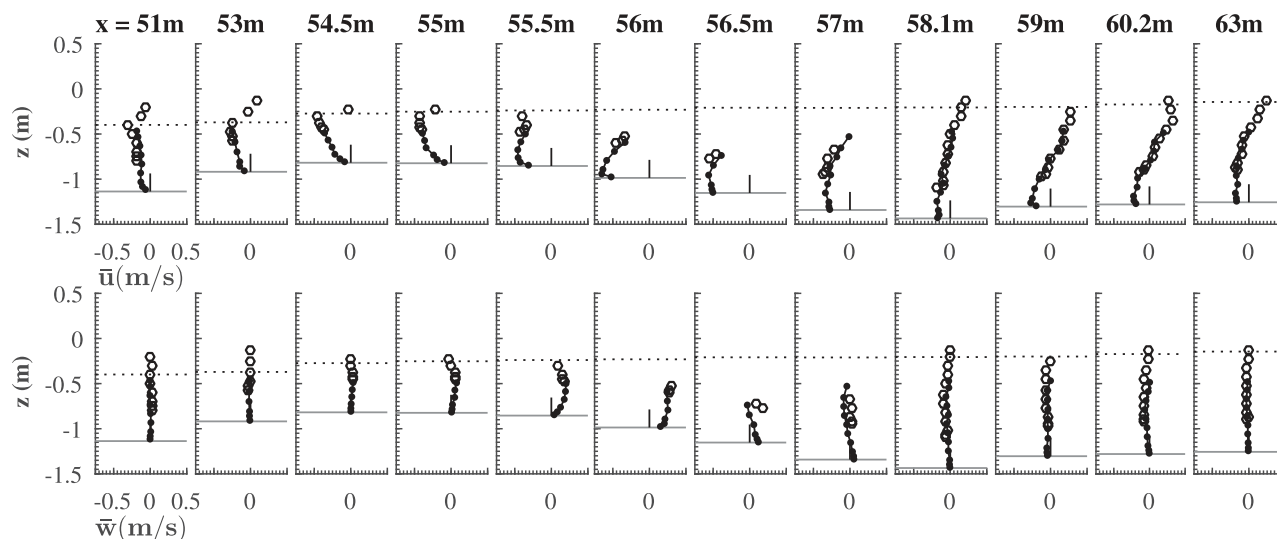
Figure 5. (top) Time-averaged horizontal and (bottom) vertical velocity along the breaker bar measured by LDA (dots) and ADV (open circles). The thick line indicates the fixed bed position and the dashed line the minimum wave trough level.

of the bubbles, time-averaged velocities are only reported below trough level, and, in the intense plunging region ($x = 55.5$–57 m), only for the bottom part of the water column. In the shoaling zone above trough level bubbles were not present, but here the ADVs were unable to measure during phases directly after the air-water transition; data could therefore not be obtained during the entire wetted flow cycle and were therefore omitted.

In the shoaling zone up to $x = 53$ m, time-averaged velocities below trough level are nearly depth-uniform and reach magnitudes up to 0.25 m/s. On the breaker bar and along the shoreward side of the bar, the magnitude of the undertow increases, due to the bar geometry and enhanced onshore mass flux above trough level related to wave breaking. A maximum horizontal velocity magnitude of around -0.65 m/s is found along the lee-side of the bar at $x = 56$ m. The undertow results in upward-directed vertical velocities along the shoreward side of the bar, reaching a maximum of 0.30 m/s at $x = 56$ m. In the trough of the bar ($x = 58.1$ m), and further onshore, the velocities are lower in magnitude as a result of increased depth and reduced onshore mass flux above trough level.

The undertow profiles in the breaking region are strongly nonuniform with depth and the vertical structure changes significantly in the cross-shore direction. At the shoreward side of the bar ($x = 56$ m), velocity magnitude increases rapidly from the bed upward, reaching a maximum at 5 cm above the bed, followed by a parabolic decrease toward the water surface. On the bar crest, ($x = 54.5$–55.0 m), the profiles increase gradually from the bed upward and reach a maximum at the trough level. A similar cross-shore variation in undertow profile can be identified on barred profiles in other studies [*Garcez Faria et al.*, 2000; *Boers*, 2005; *Govender et al.*, 2011]. In the inner surf zone, the mean flow is in the onshore direction in the upper part of the water column, as observed by *Sancho et al.* [2002] over a fixed bar in the same facility. An alternative view of the time-averaged flow pattern is presented in Figure 6, which shows vectors of the time-averaged velocities. The change in flow structure as the undertow negotiates the bar is clearly evident: on the shoreward side of the bar, the velocities are high near the bed and decrease upward; at the bar crest ($x = 55.5$ m), the velocities are approximately depth-uniform through most of the water column; on the seaward side of the bar, the velocities are highest near the top of the water column and decrease downward. The vectors also indicate a large-scale circulation cell from the breaking area into the inner surf zone, with onshore, downward-directed flow in the upper part of the water column, which reverses direction lower in the water column, leading to relatively high velocity near the bed directed offshore toward the bar.

4.2. Time-Dependent Velocities

Figure 7 shows the phase-averaged velocity vectors, composed of the time-averaged and wave-related components, at nine phases of the wave cycle. Also shown for illustration are color contours of the magnitude of the horizontal velocity component, which were obtained by interpolating the data in between the
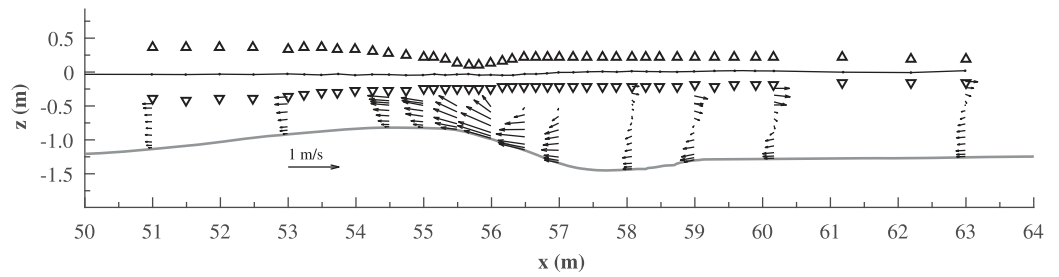
Figure 6. Time-averaged velocity vectors along the bar. Note that for clarity only ADV measured vectors above the LDA measurement positions are shown. Upward and downward triangles indicate wave crest and trough level, respectively.
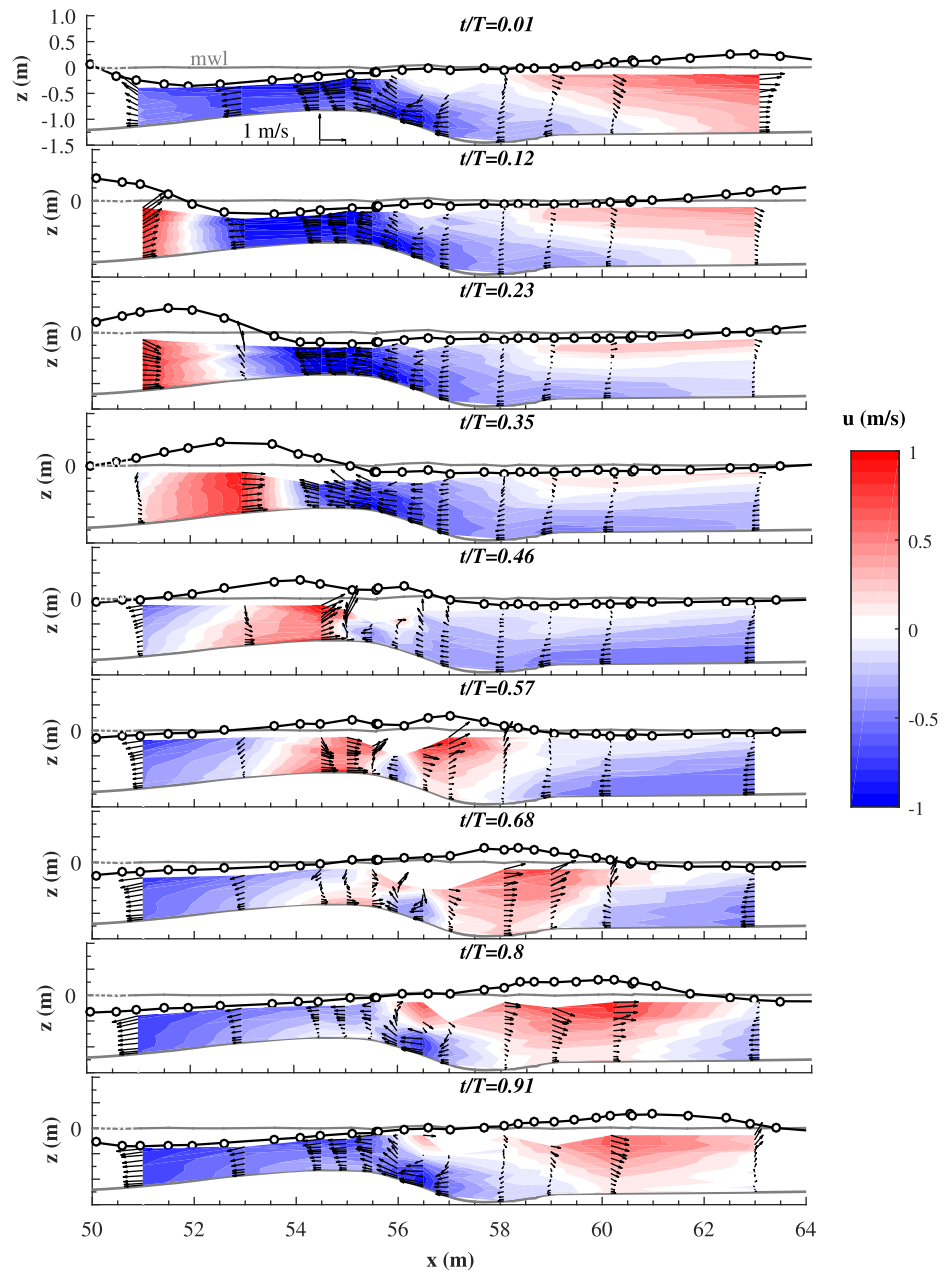

Figure 7. Instantaneous velocity vectors along the profile at nine phases during the wave cycle. The color contours indicate the magnitude of the horizontal velocity and the circles indicate the water surface elevation. $t/T=0$ corresponds to the wave zero up-crossing at $x = 50$ m.
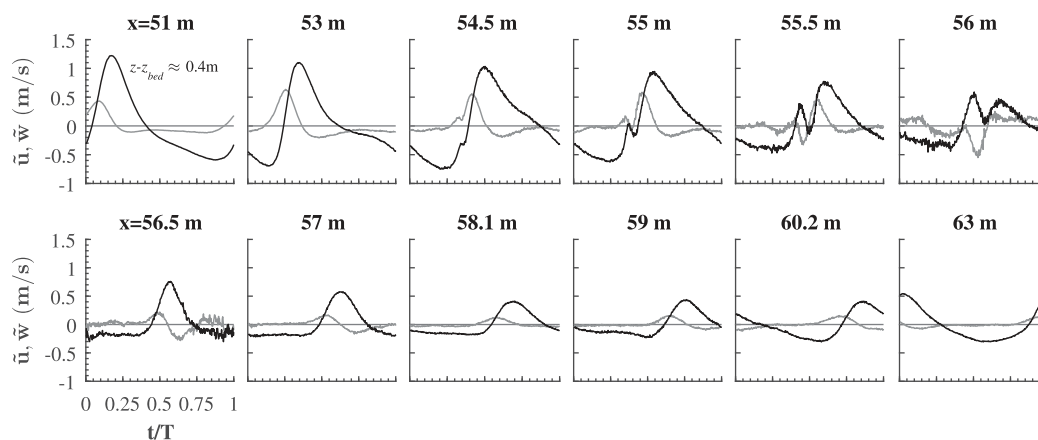
Figure 8. LDA-measured wave-related component of the horizontal (black) and vertical (gray) velocities at 0.4 m above the bed.

measurement locations. The first three phases ($t/T=0.01$ to 0.23) correspond to preplunging; the middle three ($t/T=0.35$ to 0.57) correspond to plunging and splash-up, and the last three phases ($t/T=0.68$–0.91) correspond to the propagating bore.

A complex velocity pattern results from the combination of the wave motion, the undertow, and, in the breaking area, the effects of jet penetration and push up of water. High offshore velocities occur on top of the bar crest under the wave trough, where the strong undertow and wave-related velocities are both offshore directed. On the lee-side of the bar ($x = 56$–57 m), near-bed velocities remain offshore directed throughout most of the wave cycle since the undertow exceeds the wave-related velocities (u velocities become positive for a fraction of the wave cycle only; not shown here). The gaps in the velocities around the plunge point are a consequence of the penetration of air bubbles into the water column, which is seen to increase with depth during the breaking process ($t/T=0.35-0.68$). On the shoreward side of the bar, the wave trough begins at $t/T=0.8-0.91$, and yet shows substantial onshore-directed velocities in the upper part of the water column, most likely resulting from the onshore momentum of the plunging jet. Velocities in the bar trough ($x = 58$ m) remain relatively low through most of the wave cycle, except during the phase when the bore passes ($t/T=0.68$).

Figure 8 shows the wave-related components of horizontal and vertical velocity, $\tilde{u}$ and $\tilde{w}$, at 0.4 m above the bed. This distance is sufficiently away from the bed so that the flow components are not directly influenced by the bed geometry while in the plunging area it is close enough to the bed so that the measurements do not suffer from dropouts. In the shoaling zone, $\tilde{u}$ is strongly skewed and asymmetric, typical of waves close to breaking, while $\tilde{w}$ is $\approx 90°$ out of phase with $\tilde{u}$, consistent with wave orbital motion. At $x = 54.5$–55 m, another peak occurs in both $\tilde{u}$ and $\tilde{w}$ as a result of the jet hitting the water. The peak increases shoreward until $x = 56$ m as the new wave is formed, while the secondary peak decreases in magnitude as the incoming wave dissipates. At these locations (and depths), the $\tilde{w}$ velocities under the primary crest are in (opposite) phase to $\tilde{u}$, because the incoming jet carries forward and downward momentum. It is evident that at these locations, the periodic velocities are not only driven by the orbital wave motion, but also by the organized motion of the plunging jet. *Okayasu et al.* [1986] also noted the importance of this plunging jet on the fluid motion and proposed a decoupling of the periodic velocity ($\tilde{u}$ in equation (3)) into an irrotational part related to the wave motion and a rotational part related to the vortex motion. At these locations, the vortex motion also influences the velocity skewness and asymmetry, which are both essential drivers for net sediment transport, it might therefore be difficult to predict these parameters. Moreover, the strong antiphase behavior between $\tilde{u}$ and $\tilde{w}$ further gives rise to locally high wave Reynolds stresses $-\tilde{u}\tilde{w}$ (see section 5.3). At $x = 56.5$ m, the wave reforms and the vertical velocity no longer indicates flow due to a downward-directed jet. From $x = 57.1$ to 58.1 m, the velocities decrease mainly as a result of the increase in water depth ($x = 58.1$ m is in the bar trough). Further onshore, in the inner surf zone between $x = 60.2$ and 63 m, the $\tilde{u}$ velocity changes shape from an almost purely asymmetric (sawtooth) shape to a more skewed time series.

5. Turbulence

5.1. Time-Averaged Turbulent Kinetic Energy and Turbulence Intensity

Figure 9 shows time-averaged turbulent kinetic energy $\bar{k}$, normalized by shallow water linear wave speed $(gh)^{0.5}$, where h is the local water depth, to facilitate comparison with previous studies. Phase-averaged turbulent kinetic energy per unit mass for the three-component ADV measurements is $k = \frac{1}{2}\left(\langle u'^2\rangle + \langle w'^2\rangle + \langle v'^2\rangle\right)$; for the two-component LDA measurements, the turbulent kinetic energy is calculated using $k = \frac{1.33}{2}\left(\langle u'^2\rangle + \langle w'^2\rangle\right)$, following *Svendsen* [1987]. The validity of this assumption for the two-component measurement will be discussed at the end of this section. Figure 9 also shows horizontal and vertical turbulence intensities (normalized by $(gh)^{0.5}$), defined as

$$\overline{u'}_{rms} = \overline{\sqrt{\langle u'^2\rangle}} \tag{4}$$

$$\overline{w'}_{rms} = \overline{\sqrt{\langle w'^2\rangle}} \tag{5}$$

At most locations the agreement between the LDA and ADV results is quite good, particularly since the LDA estimates of $(\bar{k}/gh)^{0.5}$ rely on the assumption of plane wake turbulence. Only at the furthest seaward and furthest shoreward locations ($x = 51$ m and 63 m, respectively), where turbulence is relatively low, is there a consistent difference between the measurements, with the ADV showing higher $(\bar{k}/gh)^{0.5}$ at both locations. This difference may well be related to additional ADV noise and the much larger sampling volume compared to the LDA. Additionally there could be a some influence of the frame, since the ADV1 measurement volume is positioned closer to the frame structure compared to LDA (cf. Figure 2). However, these differences are only apparent when the overall turbulence level is low.

Lowest $(\bar{k}/gh)^{0.5}$ is found in the prebreaking region at the most offshore location, where $(\bar{k}/gh)^{0.5}$ is almost uniformly distributed over the water depth. $(\bar{k}/gh)^{0.5}$ increases toward the breaking region, with highest values in the upper part of the water column. On top of the breaker bar, $(\bar{k}/gh)^{0.5}$ is quite uniformly distributed over the water column due to the strong vertical mixing, similar to the observations of *Scott et al.* [2005] and *Govender et al.* [2011] for plunging waves over a barred profile. At the lowest measurement position at $z - z_{bed} \approx 1$ cm, which is within the boundary layer, $(\bar{k}/gh)^{0.5}$ is about 4 times larger at the bar crest ($X = 55.5$ m) compared to the furthest offshore location ($X = 52$ m). Since peak velocities at the offshore location are the highest along the entire measurement area, it is evident that the high near-bed $(\bar{k}/gh)^{0.5}$ in the
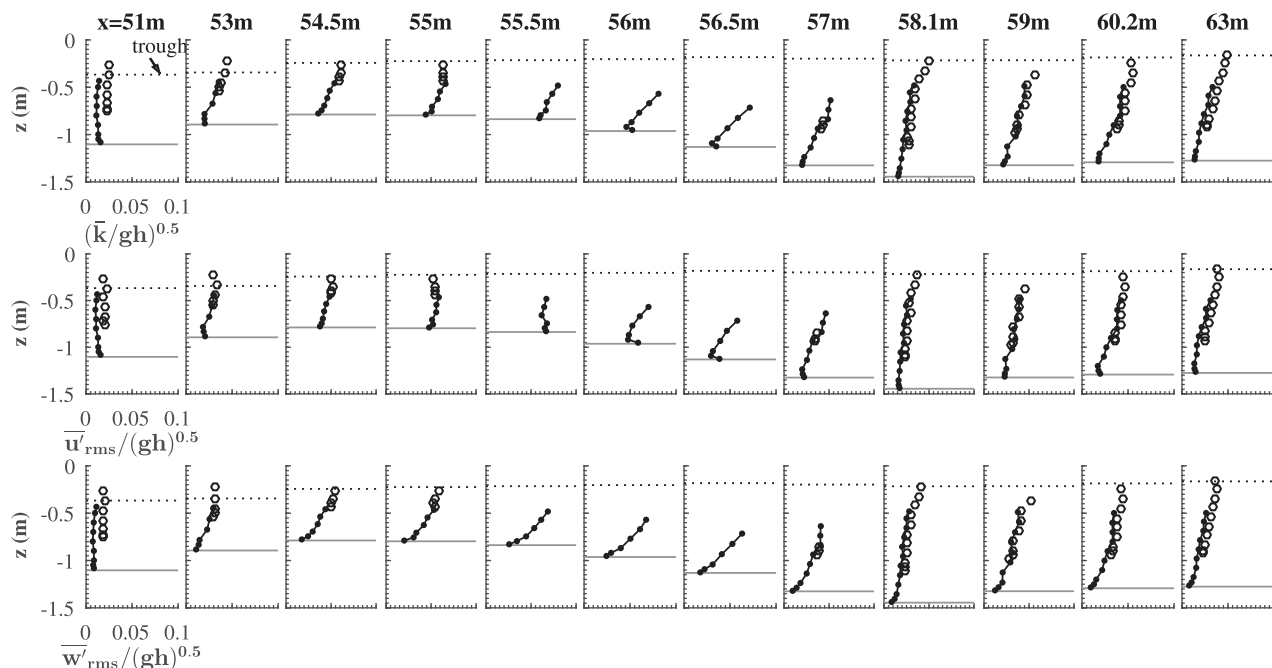

Figure 9. (top) Vertical profiles of time-averaged normalized turbulent kinetic energy, (middle) rms horizontal turbulence intensity, and (bottom) rms vertical turbulence intensity.

breaking region is the result of breaking-generated turbulence being transported toward the bed, which was also observed by *Scott et al.* [2005]. In fact, for most locations there is no distinct increase in $(\overline{k}/gh)^{0.5}$ close to the bed, which implies that bed-generated turbulence is low compared to the breaking turbulence. Exceptions are at $x = 56$ m and $x = 56.5$ m, which may be due to the increased roughness of the bed on the lee-side of the bar as a result of the curing process described previously.

On the shoreward side of the bar at $x = 56$–57 m, $(\overline{k}/gh)^{0.5}$ is highest for the uppermost measurement locations shown, even though measurements do not reach as close to the wave trough level as at other locations. There are strong gradients in the profiles at these locations, in contrast to the more depth-uniform profiles seen on top of the bar ($x = 54.5$–55.5 m). While there could be an effect of increased water depth, it is also likely that the large positive vertical component of the undertow prevents strong vertical mixing of the surface-generated TKE at these locations. In the inner surf zone, $(\overline{k}/gh)^{0.5}$ is highest near the wave trough level and decreases toward the bed, consistent with TKE profiles under spilling breakers, in which turbulence is generated in the bore above wave trough level and advances into the water column by diffusion rather than advection.

In the bar trough at $x = 58.1$ m, $(\overline{k}/gh)^{0.5}$ is low compared to the adjacent locations. *Yoon and Cox* [2010] found similarly low $\overline{k}$ levels in the bar trough of an evolving mobile-bed profile and attributed the lower values to the larger water depth, since the turbulence can spread over a larger mass of water. Another reason for lower TKE in the present case is the lower local TKE production in the upper part of the water column, since the bar trough is located between the plunging and splash-up points (Figure 4).

The vertical profiles of time-averaged horizontal turbulence intensity, $\overline{u'}_{rms}$, show a similar behavior to the $(\overline{k}/gh)^{0.5}$ profiles, except that the profiles on top of the breaker bar are even more depth-uniform. Under the plunging wave large turbulent vortices spread rapidly throughout the water column, giving rise to large $\overline{u'}_{rms}$ near the bed. By comparison, the profile of $\overline{w'}_{rms}$ show decreasing vertical turbulence intensity as the bed is approached, since the vertical turbulent fluctuations are more restricted by the bed. This behavior in $\overline{u'}_{rms}$ and $\overline{w'}_{rms}$ is notably different from spilling waves, for which $\overline{u'}_{rms}$ and $\overline{w'}_{rms}$ both show similar decreasing profiles as a result of the slow spreading of turbulence throughout the water column [*Ting and Kirby*, 1996].

The relative contribution of each of the velocity components to $\overline{k}$ is shown in Figure 10. *Townsend's* [1976] ratios for plane wake turbulence ($\overline{u'^2} : \overline{w'^2} : \overline{v'^2} = 0.42 : 0.32 : 0.26$), which according to *Svendsen* [1987]
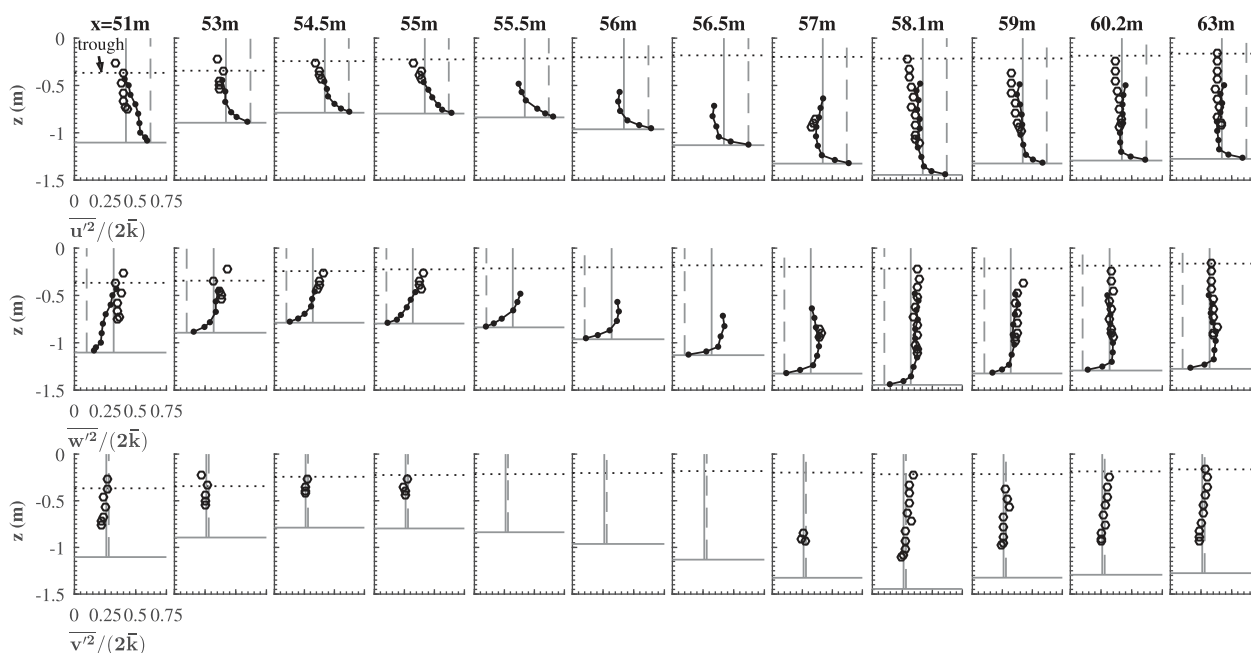

Figure 10. Ratios of time-averaged turbulence intensities. The gray vertical lines indicate *Svendsen's* [1987] ratios for surf zone turbulence: $\overline{u'^2}/2\overline{k} = 0.42$, $\overline{w'^2}/2\overline{k} = 0.32$, $\overline{v'^2}/2\overline{k} = 0.26$ and the dashed lines *Townsend's* [1976] ratios for inner boundary layer turbulence: $0.62 : 0.10 : 0.28$.

apply to surf zone turbulence, are indicated by the gray vertical lines in the figure. Generally the plane wake ratios are satisfied in the inner surf zone. The ADV measurements demonstrate the validity of applying the plane wake turbulence assumption to the present conditions since the measured $\overline{v'^2}/\overline{k'}$ ratio is quite close to 0.26, at least in those parts of the water column where ADV measurements were made. At the first location in the shoaling zone, $x=51$ m, the LDA profile in particular shows the largest deviations from the plane wake ratios, which is most likely because the turbulence at this location is no longer dominated by breaking-generated turbulence.

At all locations the contribution of $\overline{u'^2}$ becomes more dominant as the bed is approached, indicating that the turbulent eddies become more anisotropic due to the restriction on vertical velocity fluctuations near the bed. In the breaking region, the transformation to greater $\overline{u'^2}$ contributions occurs at higher elevations from the bed compared to the shoaling and inner surf zones. This suggests that the large turbulent vortices generated at breaking are advected rapidly toward the bed, retaining much of their horizontal motion, while in the inner surf zone the scale of the generated vortices and the vertical advection is much smaller, and the eddies therefore remain more isotropic upon reaching the bed. Close to the bed, within the wave boundary layer, the ratios are in good agreement with the ratios given by *Townsend* [1976] for inner boundary layer turbulence.

5.2. Time-Dependent Turbulent Kinetic Energy

Figure 11 shows k along the profile at different phases of the wave cycle; the phases are the same as those in Figure 7. Large k occurs throughout the flow cycle in the breaker area at the bar crest and the shoreward side of the bar. Largest k is expected to be produced when the jet hits the water at $t/T \approx 0.35$, although the peak itself is not directly measurable due to the presence of the bubbles. At the next phase, $t/T=0.46$, higher levels of k occur close to the bed on top of the bar. Such rapid vertical mixing near the plunge point was also found by *Scott et al.* [2005] and *Govender et al.* [2011] and is also typical for plunging waves on plane sloping beaches where the water depth is relatively shallow [e.g., *Ting and Kirby*, 1994; *Govender et al.*, 2002]. During the remainder of the crest half cycle (until $t/T=0.8$), the region of large k spreads in the onshore direction and downward along the shoreward side of the bar. The region of high k persists throughout the trough half cycle, during which it is transported in the offshore direction, reaching as far as $x = 52$ m at $t/T=0.23$. At $x = 58$ m in the bar trough, in between the plunging and splash-up points, k remains low over the entire depth and during the entire wave cycle. Further onshore in the inner surf zone, k is largest when the wave crest passes ($t/T = 0.8$–0.12), but vertical spreading of k into the water column is not as pronounced as in the breaking region, behavior that is similar to that observed under spilling waves.

Figure 11 shows that breaking-generated k spreads throughout the water column and reaches the bed in the breaking area. To illustrate better the near-bed k behavior, Figure 12 presents time series of k at 5 cm (near-bed) and 40 cm (free-stream) above the bed. At all locations, k is largest higher up in the water column. Maximum k is reached at $x = 55.5$–56 m, in the shallowest water close to the plunging location and reduces with distance onshore and offshore from the breaker area. Peak k in this region is an order of magnitude higher than peak k at the most offshore location ($x = 51$ m), and it remains high throughout the whole of the wave cycle. The strongest time-variation is observed in the breaking area ($54.5 < x < 58.1$ m) and at higher elevations above the bed, for which the difference between the minimum and maximum k is about a factor 3. Closer to the bed and away from the breaking area the time-variation in k is considerably weaker. In the breaking area, k does not reduce to zero after the high peaks but remains at a relatively high level which indicates that turbulence does not decay fully during the wave cycle. This relatively high "residual" k therefore indicates that turbulence partly sustains into the subsequent wave cycle, as also indicated by *Svendsen* [1987]. Comparison of the phase-behavior of k with u shows that the peak in k is in phase with the primary crest in u at $x = 55$ m. Further onshore ($x=56.5-57$ m), there is a substantial time-lag between k and u, such that at 0.4 m the peak in k occurs during the wave trough phase. The phase behavior between $\tilde{u}$ and k is further investigated in section 6.1.

5.3. Reynolds Stress

Contour plots of the turbulent Reynolds shear stress $-\overline{\langle u'w' \rangle}$ and the wave Reynolds shear stress $-\overline{\langle \tilde{u}\tilde{w} \rangle}$ are shown in Figure 13. Turbulent Reynolds stress is highest and positive in the breaking area, meaning that momentum transfer is downward and onshore or upward and offshore. $-\overline{\langle u'w' \rangle}$ is much lower in the shoaling area and in the inner surf zone.
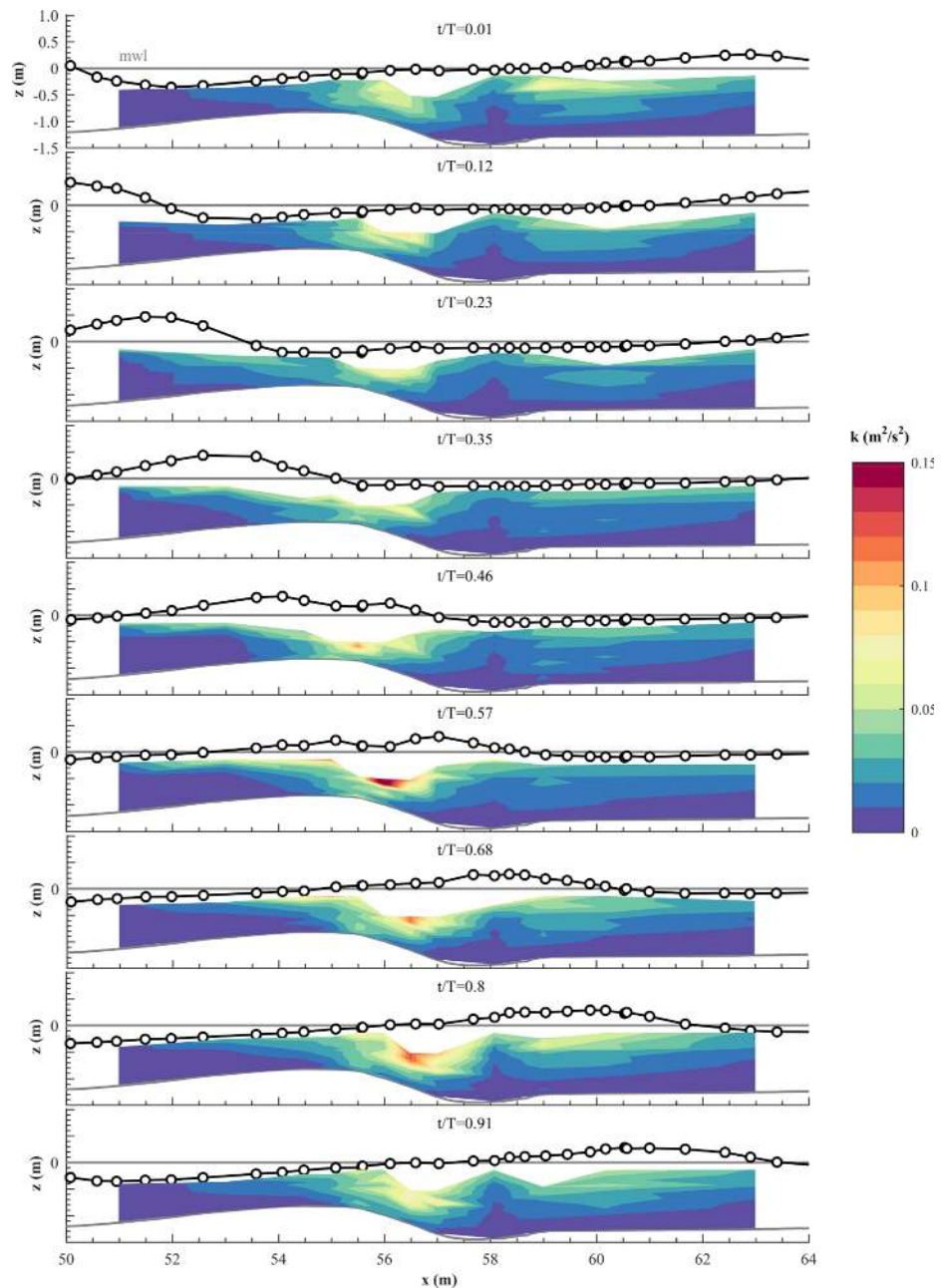
Figure 11. Phase-averaged turbulent kinetic energy at nine phases during the wave cycle. Note that the contours are obtained by interpolation of the data at the 12 cross-shore measurement profiles.

The wave Reynolds shear stress $-\overline{\langle \tilde{u}\tilde{w} \rangle}$ is generally higher than the turbulent stress, except on the shoreward side of the bar where the jet penetrates the upper water column, and shows more cross-shore variation than the turbulent stress In the shoaling zone $-\overline{\langle \tilde{u}\tilde{w} \rangle}$ is negative, but on the shoreward side of the bar $-\overline{\langle \tilde{u}\tilde{w} \rangle}$ is positive lower in the water column, with highest values close to the bed; in the inner surf zone $-\overline{\langle \tilde{u}\tilde{w} \rangle}$ is mostly negative but is positive in the upper part of the water column at $x \approx 60.2$ m. The high $-\overline{\langle \tilde{u}\tilde{w} \rangle}$ on the shoreward side of the bar is largely due to the measurement orientation since we measure the horizontal and vertical velocity components of the wave velocity, while the flow oscillates parallel to the bed, leading therefore to high correlation between $\tilde{u}$ and $\tilde{w}$. Some part of the high $-\overline{\langle \tilde{u}\tilde{w} \rangle}$ may additionally be due to the coherence between $\tilde{u}$ and $\tilde{w}$ resulting from the jet motion.
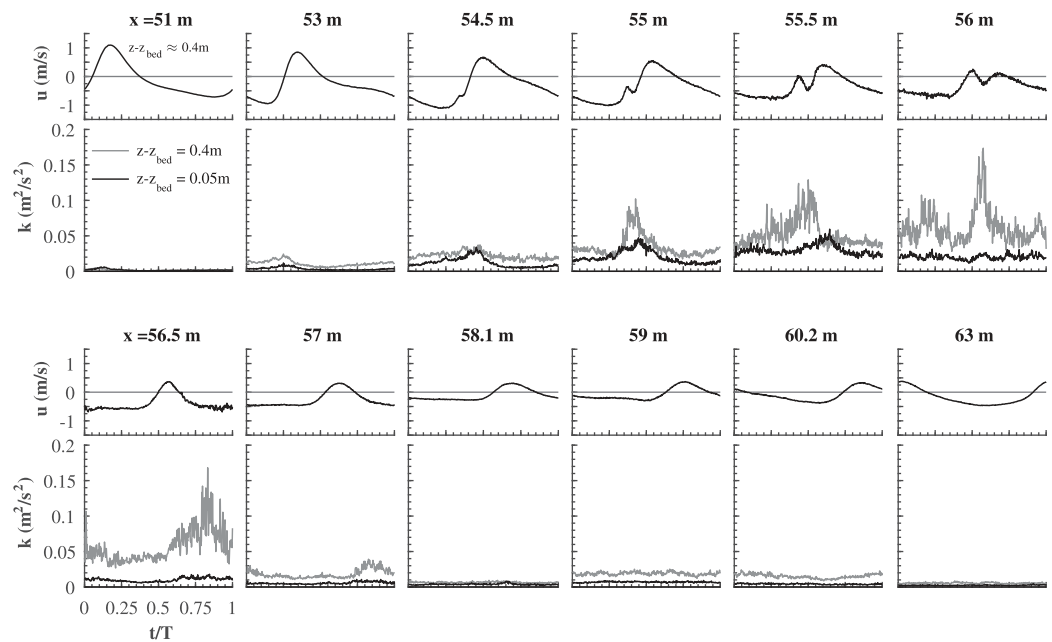
Figure 12. Time series of k at approximately 0.05 m (black line) and 0.4 m (gray line) above the bed; the LDA-measured horizontal velocity at approximately 0.4 m is also shown for reference.

The combined turbulent and wave Reynolds stresses are highest on the shoreward slope of the bar. The combined stresses are positive over most of the water column, which agrees with the positive $\partial \overline{u}/\partial z$ seen in the undertow profiles at these locations (Figure 5). Consequently, the high positive turbulent and wave Reynolds stresses in the breaking region contribute to the strong offshore-directed near-bed undertow
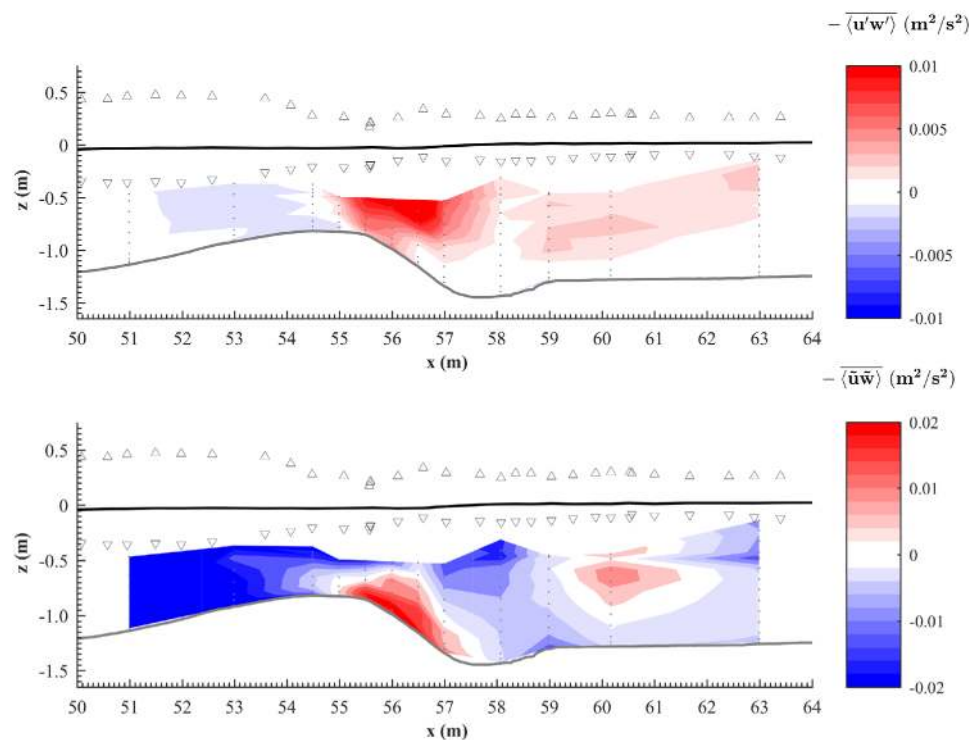

Figure 13. (top) Time-averaged turbulent Reynolds shear stress $-\overline{\langle u'w' \rangle}$ and (bottom) time-averaged wave Reynolds stress $-\overline{\langle \overline{u}\overline{w} \rangle}$. The dots indicate the measurement locations; triangles indicate the maximum (crest) and minimum (trough) water surface elevation.

velocity along the shoreward slope of the breaker bar, which leads to a high negative $\partial \overline{u}/\partial z$ by the under-tow in the lowest part ($\sim$0.10 m) of the water column.

6. Turbulent Kinetic Energy Transport, Production, and Dissipation

6.1. Transport of Turbulent Kinetic Energy

The turbulent kinetic energy budget is written as [*Tennekes and Lumley*, 1972]

$$\frac{\partial k}{\partial t} + \frac{\partial \langle u \rangle k}{\partial x} + \frac{\partial \langle w \rangle k}{\partial z} = -\frac{1}{\rho}\left(\frac{\partial \langle u'p' \rangle}{\partial x} + \frac{\partial \langle w'p' \rangle}{\partial z}\right) - \left(\frac{\partial \langle k'u' \rangle}{\partial x} + \frac{\partial \langle k'w' \rangle}{\partial z}\right) + \mathcal{P} - \varepsilon \tag{6}$$

in which k' is the instantaneous turbulent kinetic energy, k is the ensemble-averaged value, and p' is the turbulent pressure fluctuation. Here we assume two-dimensionality of the flow ($\partial/\partial y = 0$) and neglect viscous transport, which is small for high Reynolds number flows. Terms contributing to the time-rate-of change of k (term 1) are advection (terms 2 and 3), diffusive transport due to pressure fluctuations (terms 4 and 5), diffusive transport due to turbulent velocity fluctuations (terms 6 and 7); $\mathcal{P}$ and ε are turbulence production and dissipation, respectively, and are discussed in the next section.

Ting and Kirby [1995] and *De Serio and Mossa* [2006] showed that under plunging breakers in a small-scale wave flume the advective transport of k is onshore directed due to the high levels of k occurring during the wave crest phase compared to the trough phase. Turbulent diffusive transport (terms 6 and 7) was found to be onshore and downward directed, and of similar magnitude to the advective transport. For irregular waves, *Boers* [2005] found offshore transport of k as a result of the undertow and a wave-related transport that was onshore directed in the upper part of the water column and offshore directed in the bottom part
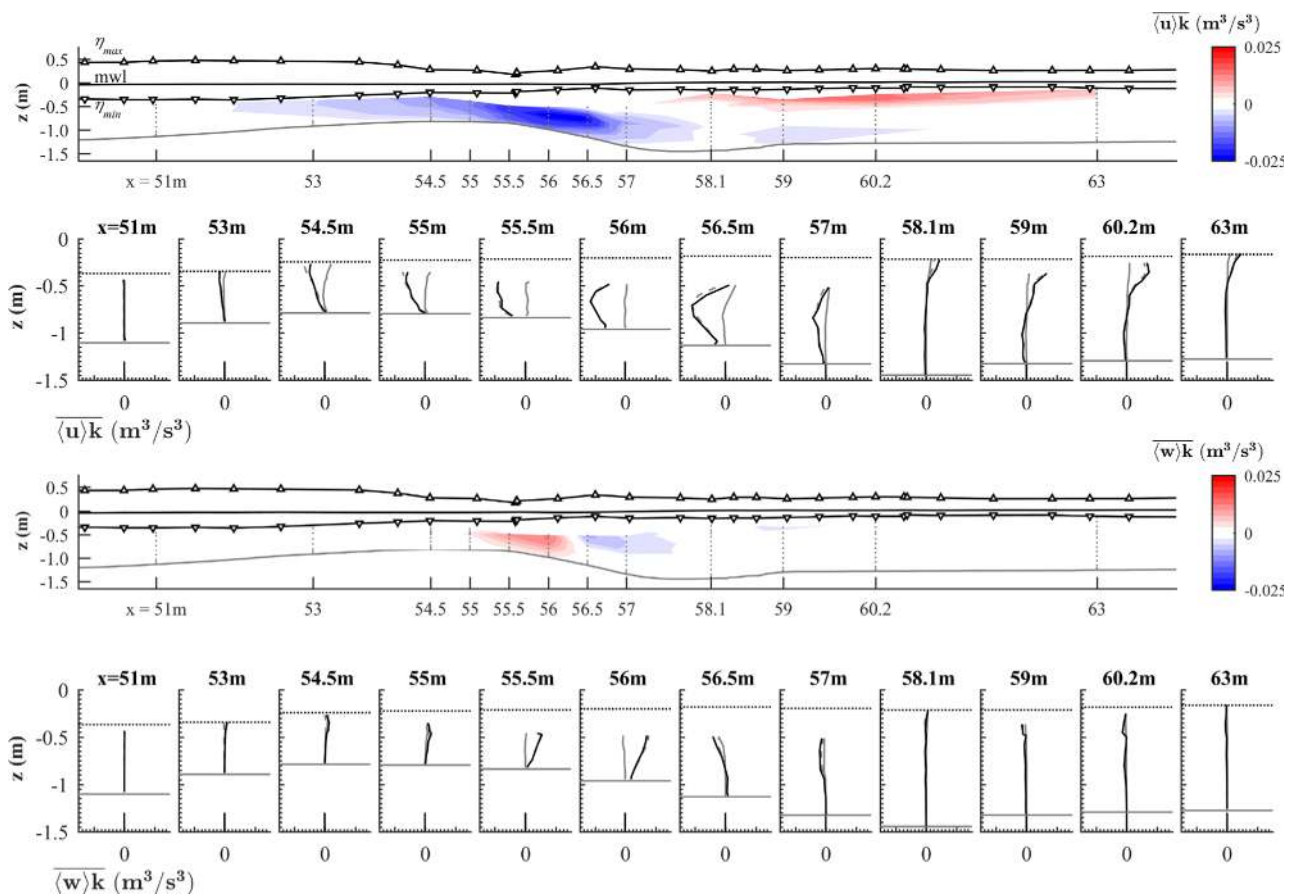

Figure 14. Time-averaged advection of turbulent kinetic energy: (top) $\overline{\langle u \rangle k}$ and (bottom) $\overline{\langle w \rangle k}$. The gray profiles represent the wave-related (solid) and current-related (dashed) transport component.

because of the phase difference between turbulence generation at the crest and turbulence arrival near the bed during the wave trough phase.

Here we consider only the time-averaged advective fluxes, $\langle u \rangle k$ and $\langle w \rangle k$, and time-averaged diffusive fluxes $\overline{u'k'}$ and $\overline{w'k'}$. Vertical profiles of the advective terms are shown in Figure 14. There is strong horizontal advection in the offshore direction on the downward slope of the bar as a result of the strong undertow.

In the inner surf zone k is mainly transported in the onshore direction higher up in the water column. The horizontal advective flux can be decomposed into a wave-related flux $\overline{\tilde{u}k}$ and a current-related flux $\overline{\overline{u}k}$; similarly the vertical component can be decomposed into $\overline{\tilde{w}k}$ and $\overline{\overline{w}k}$. Profiles of both contributions are shown in Figure 14 which demonstrate that almost all advection is related to the undertow. The low contribution of the wave-related component along the profile, with the exception of the breaking area, can be associated to the generally small temporal variation in k at these locations.

The sign of $\overline{\tilde{u}k}$ and $\overline{\tilde{w}k}$ can be interpreted as the phase correlation between the orbital motion and time-varying k, with a positive (negative) sign indicating higher TKE during the crest (trough) phase. Thus, negative flux near the bed means that there is a phase difference between TKE generation at the surface and TKE arrival near the bed. The level at which the transition from onshore-directed to offshore-directed flux takes place depends strongly on the wave conditions. Figure 15 shows the wave-related fluxes in more detail. Note that the color scale is a factor 10 smaller compared to Figure 14. Figure 15 shows a positive phase correlation near the water surface, consistent with generation of turbulence at the wave crest. Negative $\overline{\tilde{w}k}$ correlation reveals downward advection around the shoreward side of the bar, which can be related to the penetration of the plunging jet at this location. In the shoaling zone $\overline{\tilde{w}k}$ is positive in the upper part of the water column.

In the lower half of the water column, predominantly negative $\overline{\tilde{u}k}$ shows that breaking-generated turbulence arrives at the bed during the offshore half-cycle, implying a phase lag between the turbulence generation at the surface and turbulence arrival at the bed similar to *Boers* [2005]. A small region of positive $\overline{\tilde{u}k}$ occurs throughout the water column at the bar crest ($x = 55$–56 m). At this location, highest TKE occurs during the crest half-cycle, which is likely due to the rapid mixing of breaking-induced TKE by the plunging jet.
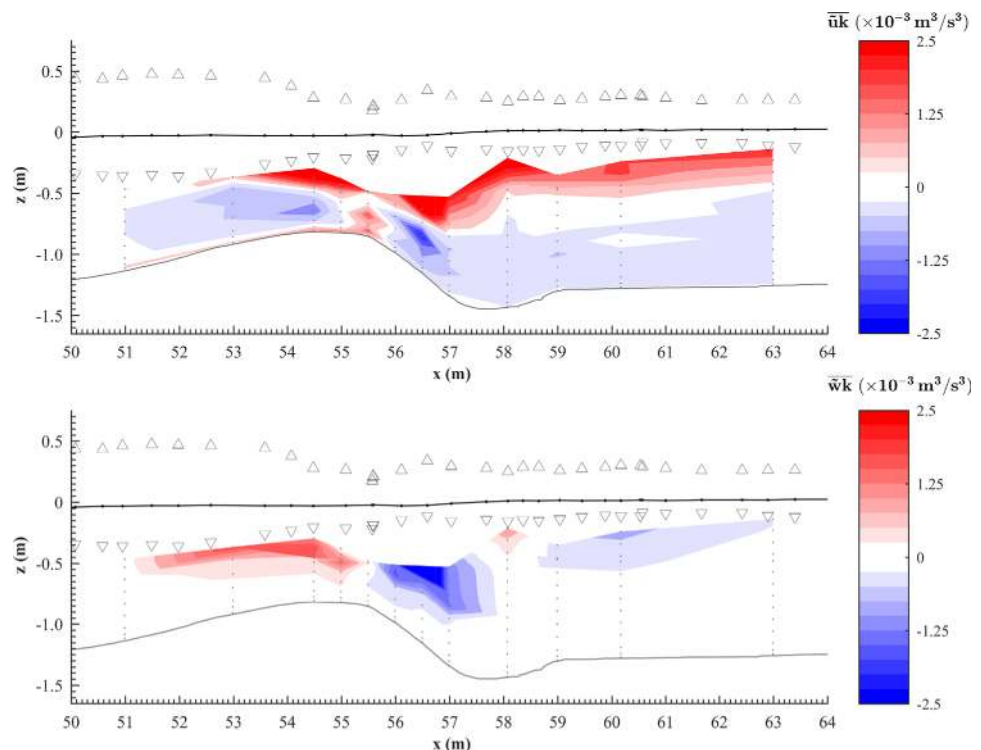

Figure 15. Time-averaged wave-related TKE flux. (top) horizontal component $\overline{\tilde{u}k}$; (bottom) vertical component $\overline{\tilde{w}k}$; triangles indicate the maximum (crest) and minimum (trough) water surface elevation.
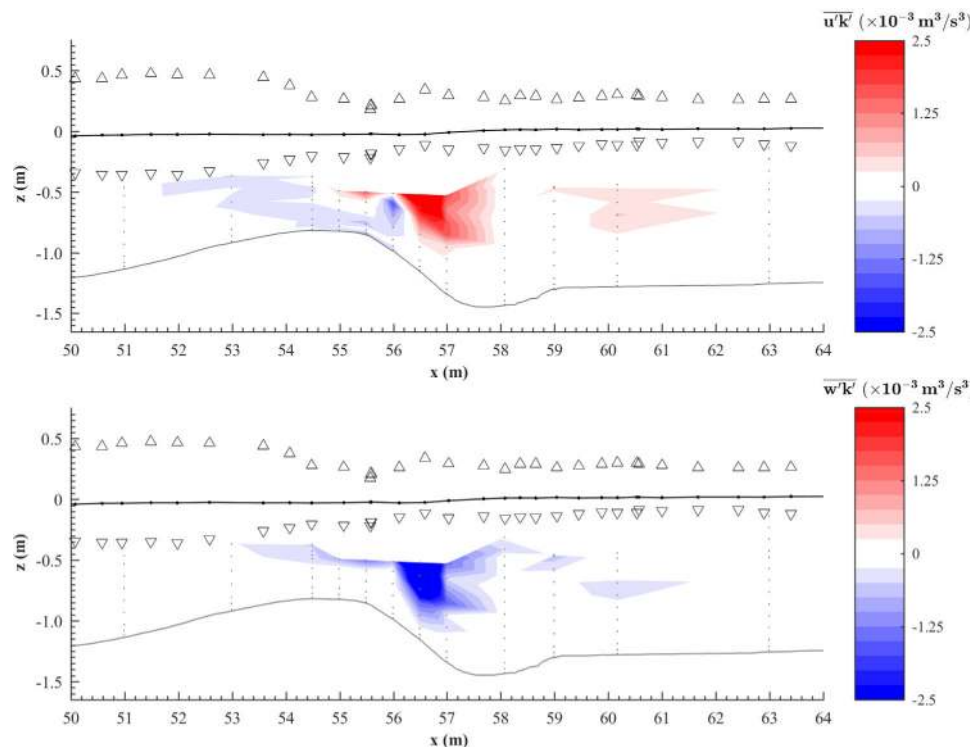
Figure 16. Contour plot of turbulent diffusive fluxes: (top) $\overline{k'u'}$ and (bottom) $\overline{k'w'}$; triangles indicate the maximum (crest) and minimum (trough) water surface elevation.

Very close to the bed on the offshore side and on top of the bar a small layer of positive $\overline{\tilde{u}k}$ can be seen as a result of bed-generated TKE being in phase with the wave-related velocities.

Figure 16 shows contours of the time-averaged turbulent diffusive fluxes $\overline{k'u'}$ and $\overline{k'w'}$. The diffusive fluxes are concentrated around the breaking point where they are onshore and downward directed. The magnitude of the diffusive fluxes is considerably smaller than the advective fluxes.

6.2. Production and Dissipation

To understand further the spatial and temporal variation in TKE, the production and dissipation terms of the time-averaged TKE balance equation are examined. Again, assuming two-dimensional flow, $\mathcal{P}$ in equation (6) can be written as [e.g., *Ting and Kirby*, 1995; *Kimmoun and Branger*, 2007]:

$$\mathcal{P} = -\langle u'w'\rangle\frac{\partial\langle u\rangle}{\partial z} - \langle u'w'\rangle\frac{\partial\langle w\rangle}{\partial x} - \langle u'^2\rangle\frac{\partial\langle u\rangle}{\partial x} - \langle w'^2\rangle\frac{\partial\langle w\rangle}{\partial z} \tag{7}$$

in which the first two terms are production due to the shear stresses and the latter two terms are the production due to normal stresses. The second term is neglected since the data showed that $|\frac{\partial\langle w\rangle}{\partial x}| \ll |\frac{\partial\langle u\rangle}{\partial z}|$. Continuity requires that $\frac{\partial\langle u\rangle}{\partial x} = -\frac{\partial\langle w\rangle}{\partial z}$, which allows the normal stress contributions to be rewritten as $-\left(\langle w'^2\rangle - \langle u'^2\rangle\right)\frac{\partial\langle w\rangle}{\partial z}$.

Turbulence dissipation, ε in equation (6), can be estimated by matching velocity spectra at inertial range frequencies to theoretical models. In the surf zone, where turbulence is advected by wave-related and time-averaged velocities, the time-averaged dissipation rate, $\overline{\varepsilon}$, can be obtained following *Trowbridge and Elgar* [2001]:

$$\overline{\varepsilon}(f) = \left[\frac{55}{18}C_k^{-1}\overline{u}^{-2/3}(2\pi f)^{5/3}I\left(\frac{\tilde{u}_{\mathrm{rms}}}{\overline{u}}\right)^{-1}P_{uu}(f)\right]^{3/2} \tag{8}$$

with

$$I\left(\frac{\tilde{u}_{rms}}{\overline{u}}\right) = \frac{1}{\sqrt{2\pi}}\left(\frac{\tilde{u}_{rms}}{\overline{u}}\right)^{2/3}\int_{-\infty}^{\infty}\left[x^2 + 2\frac{\overline{u}}{\tilde{u}_{rms}}x + \frac{\overline{u}^2}{\tilde{u}_{rms}}\right]^{1/3}\exp\left(-\frac{x^2}{2}\right)dx \qquad (9)$$

In equation (8), $P_{uu}(f)$ is power spectral density for u, f is frequency; $C_k = 1.5$ is the Kolmogorov constant. The *Trowbridge and Elgar* [2001] model relies on Taylor's frozen turbulence hypothesis and assumes that measured turbulent fluctuations relate to horizontal advection of locally isotropic turbulence. Equation (8) has been applied to velocities under breaking waves in both field [e.g., *Raubenheimer et al.*, 2004] and laboratory [*Yoon and Cox*, 2010] conditions.

The dissipation analysis was restricted to the LDA measurements because ADV data suffered from acoustic noise contributions at inertial subrange frequencies. $P_{uu}(f)$ and $\overline{\varepsilon}(f)$ were calculated for each wave in a time series, using LDA data that were linearly interpolated to a regular time-interval with temporal resolution equal to the mean sampling rate over each wave, which ranges between 100 and 600 Hz. Following *Feddersen et al.* [2007], $\overline{\varepsilon}(f)$ was averaged over all frequencies in the inertial subrange by taking the log mean to give $\overline{\varepsilon}$. To ensure the validity of Taylor's hypothesis, even at elevations close to the bed where eddies are strongly anisotropic, the analysis was restricted to frequencies >50 Hz where $P_{uu}(f)$ followed a $-5/3$ slope. The high data rate of the LDA enables a sufficient amount of data points for a reliable estimate of $\overline{\varepsilon}$. Estimates of $\overline{\varepsilon}$ were then ensemble-averaged over all the waves within the time series. Another spectral method to get estimates of ε is to apply an inertial-subrange model to the wave number spectra obtained from spectral analysis of u' measured over a short-duration time-interval, during which the mean velocity is assumed constant [following *George et al.*, 1994]. Dissipation results obtained from this method were of the same order of magnitude and showed very similar cross-shore and vertical variation as those obtained based on equation (8).

Profiles of time-averaged production and dissipation are shown in Figure 17. Note that there is some scatter in $\overline{\mathcal{P}}$ since its calculation is sensitive to the time-dependent velocity gradients; at some elevations this leads to negative values of $\overline{\mathcal{P}}$ (not shown). $\overline{\mathcal{P}}$ generally decreases from the water surface downward at each cross-shore location, which is consistent with the decrease in the magnitudes of $-\overline{\langle u'w'\rangle}$ with depth. Large production in the region between wave crest and wave trough level is expected [*Melville et al.*, 2002; *Kimmoun and Branger*, 2007], but could not be measured in the present study. A local increase in production near the bed occurs at all locations and relates likely to bed shear. At free-stream elevations in the middle of the water column, highest production rates are found in the breaking region ($x = 55.5$–56.5 m). This is explained by the combination of strongly anisotropic turbulence, large magnitudes of $-\overline{\langle u'w'\rangle}$, and large velocity shear due to horizontally and vertically varying undertow velocities.
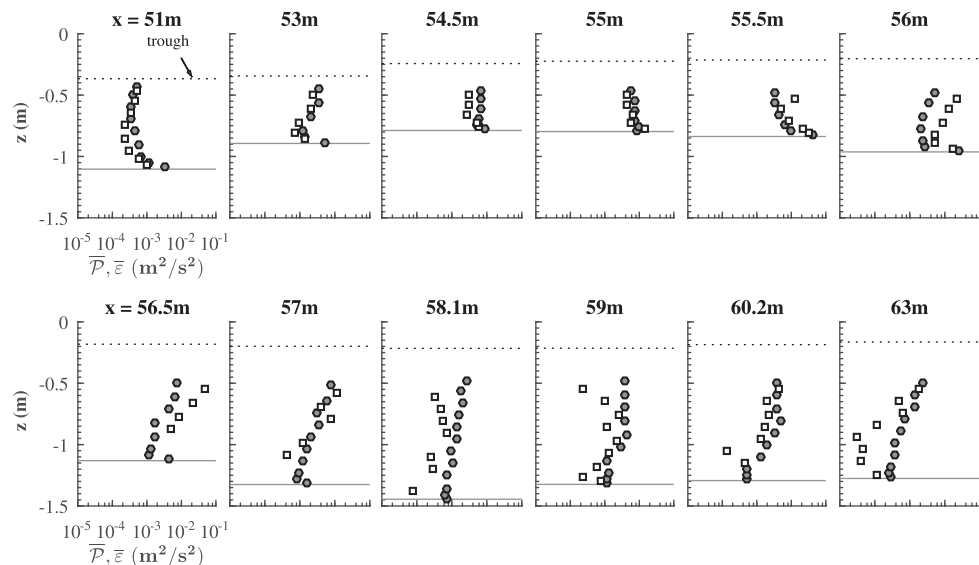

Figure 17. Time-averaged turbulence production (squares) and dissipation rates (circles) along the barred profile.

The vertical profile of $\bar{\varepsilon}$ typically decreases from the water surface downward, followed by an increase close to the bed, which is consistent with previous observations of dissipation rates under breaking waves in the field [*George et al.*, 1994; *Trowbridge and Elgar*, 2001; *Bryan et al.*, 2003] and laboratory [*Yoon and Cox*, 2010; *Brinkkemper et al.*, 2016]. Nondimensional dissipation rates, $\bar{\varepsilon}/(g^3 h)^{1/2}$, in the present study vary between 2.0×10^{-5} and 2.0×10^{-4}, which is similar to field observations [e.g., *Feddersen and Trowbridge*, 2005]. Production exceeds dissipation throughout the water column at locations near the plunge point ($x = 55.5$–56.5 m). This suggests that large TKE magnitudes in the breaking zone should not only be attributed to turbulence production at the water surface but also to production inside the water column. This also explains why net vertical advection of TKE at these locations is upward. At shoaling and in the inner surf zone, dissipation exceeds production. This likely relates to the arrival of TKE that is not produced locally, but is generated by wave breaking and transported horizontally offshore (to shoaling zone) or vertically downward (in the inner surf zone).

7. Discussion

The present paper reveals relatively high "residual" turbulence in the breaking region, i.e., turbulence does not fully dissipate within one wave cycle. This differs from the strong intrawave variation in TKE which reduces almost to zero within a cycle observed for plunging waves over plane beach slopes in small-scale wave flumes [e.g., *Ting and Kirby*, 1994; *De Serio and Mossa*, 2006; *Kimmoun and Branger*, 2007]. Froude-scaling principles should be considered to intercompare the observations from differently sized wave flumes [*Stive*, 1985]. Applying Froude-scaling, whereby the wave period T is scaled with $n^{0.5}$, where n is the geometric scaling factor based on wave height H, it follows that the studies of *Ting and Kirby* [1994] and *De Serio and Mossa* [2006] involved waves with (scaled) periods which exceed T in the present study by a factor 3 to 4. This much larger wave period could explain the absence of a significant level of residual turbulence which results in a much larger intrawave variation in TKE in these studies compared to the present experiment.

However, the wave condition by *Kimmoun and Branger* [2007] is very similar to the present study when Froude-scaled (about 10% difference in terms of scaled T), but still shows an intrawave variation in TKE that appears significantly higher than that observed in the present study. The major difference between the present study and that of *Kimmoun and Branger* [2007] is that *Kimmoun and Branger*'s experiment was conducted using a plane sloping beach experiment. The wave in the present experiment is breaking over a barred bed profile, which likely affects turbulence in the water column in two ways: first, for waves breaking over a bar the plunge point is located in relatively deep water, i.e., above the bar trough. Consequently, for a barred profile, the vertical length scale of the breaking-induced vortices is less restricted by the local water depth than for a plane sloping beach where the plunge point is located in relatively shallower water. The restricted length scale of vortices on a plane sloping beach would favour turbulent dissipation rates and enhance intrawave variation in TKE. Second, the barred profile contributes to the cross-shore nonuniformity of periodic and time-averaged (undertow) velocities. It follows from equation (7) that the associated strain rates $\frac{\partial \langle u \rangle}{\partial x}$ and $\frac{\partial \langle w \rangle}{\partial z}$ contribute to turbulence production. Indeed, the measurements reveal significant production in the water column (Figure 17) which likely reduces the intrawave variation in k.

These findings would imply that breaking-generated TKE under plunging waves over barred bed profiles, i.e., on natural beaches, has significantly lower temporal variability than expected based on plane-sloping bed experiments. It should be noted that the present breaker bar is not fully representative for field conditions: the bar was shaped through sand transport driven by monochromatic waves, which induce higher cross-shore transport gradients than equivalent irregular waves. Consequently, the crest of the bar is sharper and the shoreward slope between bar crest and trough is steeper compared to breaker bars on natural beaches [see also chap. 6 in *van der Zanden*, 2016]. A more systematic experimental or numerical investigation, using the same breaking-wave condition for a barred and a plane-sloping beach, seems useful for a more in-depth investigation of the breaker bar effects on time-varying and time-averaged turbulence. As argued by *Ting and Kirby* [1994], since turbulent vortices keep sand grains in suspension, the transport of TKE resembles the transport of suspended sediment. For the present wave condition, the transport of turbulence is primarily advective and is dominated by the current-related component $\bar{u}k$. The net transport of TKE seen here does indeed resemble the net transport of suspended sediment seen in *van der Zanden et al.*

[2016]: at outer-flow elevations the transport is dominated by the current-related advection component and the wave-related advection forms a minor contribution. This relates to the low intrawave variability of TKE for the present wave condition: TKE is continuously high, what restricts the intrawave settling of suspended sediment particles.

It should be noted that higher temporal variability in k may be expected for irregular waves and waves with longer periods. Consequently, $\overline{uk}$ (Figure 15) may still contribute to the breaking turbulence effects on sediment transport and sandbar morphodynamics at natural beaches. Specifically, the detailed spatial distributions of $\overline{uk}$ in Figure 15 show that at most locations breaking-generated turbulence arrives at the bed during the wave trough phase, which would likely contribute to offshore-directed wave-related sediment transport. An exception is at the bar crest: here, near-bed turbulence is highest during the wave crest phase and would therefore promote onshore-directed wave-related sediment transport.

8. Conclusion

A large-scale wave flume experiment was carried out involving a plunging breaking wave over a fixed barred beach profile. Water surface elevations were measured along the wave flume and vertical profiles of velocity and turbulence were measured using a Laser Doppler Anemometer and Acoustic Doppler Velocimeters at 12 locations along the breaker bar. The following are the main conclusions from the study:

1. Undertow profiles show strong cross-shore variation with highest undertow velocities reached on the shoreward side of the bar, where maximum velocities reach 0.8 m/s. In the inner surf zone, and across the shoreward side of the bar, the highest offshore directed velocities occur near the bed, while on top of the bar and in the shoaling zone the highest offshore velocities occur in the upper part of the water column. A circulation cell occurs between the breaking area and the inner surf zone.
2. Vertical profiles of time-averaged turbulent kinetic energy ($\overline{k}$) show largest $\overline{k}$ on the shoreward side of the bar where the jet penetrates the water column. The $\overline{k}$ profiles show a strong vertical gradient at these locations with $\overline{k}$ decreasing downward. The limited vertical mixing of $\overline{k}$ is a result of the upward-directed advection of $\overline{k}$ due to the strong undertow on the shoreward side of the bar. On the bar crest, $\overline{k}$ is more uniformly distributed over the water depth.
3. Time-dependent k in the breaking area shows a high level of "residual" turbulence when compared to previous similar (Froude-scaled) plunging wave experiments on plane beach profiles. This high residual turbulence is likely caused by the presence of the bar, which reduces local turbulence dissipation and increases local production within the water column.
4. The Reynolds shear stress in the near-bed region is dominated by the wave-related Reynolds shear stress except on the shoreward face of the bar where the turbulent Reynolds shear stress generated in the plunging zone affects the near-bed region.
5. Time-averaged advection of k is dominated by the current-related flux $\overline{uk}$, resulting in a strong offshore-directed flux on the shoreward side and crest of the bar. The wave-related advective fluxes $\widetilde{uk}$ and $\widetilde{wk}$ are an order of magnitude smaller compared to the current-related fluxes. The turbulent diffusive flux is an order of magnitude lower than the current-related flux and is only significant on the shoreward side of the bar.

    In the upper part of the water column, $\widetilde{uk}$ is onshore directed; closer to the bed it is offshore directed at most locations, indicating a phase lag between turbulence generation during the wave crest and turbulence arrival near the bed during the wave trough. An exception is the breaker bar crest, where near-bed $\widetilde{uk}$ is positive. Hence, time-varying turbulence may locally promote wave-related transport rates in either onshore or offshore direction, depending on the location across the wave breaking region.
6. Time-averaged turbulence production and dissipation are of similar magnitude in the breaking area, while dissipation dominates in the shoaling and inner surf zones. Production is not only significant near the water surface but also in the water column due to strong horizontal and vertical velocity gradients.

The detailed data set presented in this paper can be used to validate high-resolution numerical models and develop models to predict cross-shore hydrodynamics.

References

Battjes, J. A. (1988), Surf-zone dynamics, *Annu. Rev. Fluid Mech.*, *20*, 257–293.

Boers, M. (2005), Surf zone turbulence, Phd thesis, TU Delft, Netherlands.

Brinkkemper, J. A., T. Lanckriet, F. Grasso, J. A. Puleo, and B. G. Ruessink (2016), Observations of turbulence within the surf and swash zone of a field-scale sandy laboratory beach, *Coastal Eng.*, *113*, 62–72.

Bryan, K. R., K. P. Black, and R. M. Gorman (2003), Spectral estimates of dissipation rate within and near the surf zone, *J. Phys. Oceanogr.*, *33*, 979–993.

Chang, K. A., and P. L.-F. Liu (1999), Experimental investigation of turbulence generated by breaking waves in water of intermediate depth, *Phys. Fluids*, *11*(11), 3390–3400.

Cox, D. T., and N. Kobayashi (2000), Identification of intense, intermittent coherent motions under shoaling and breaking waves, *J. Geophys. Res.*, *105*(C6), 14,223–14,236.

De Serio, F., and M. Mossa (2006), Experimental study on the hydrodynamics of regular breaking waves, *Coastal Eng.*, *53*(1), 99–113.

Drazen, D. A., and W. K. Melville (2009), Turbulence and mixing in unsteady breaking surface waves, *J. Fluid Mech.*, *628*, 85–119.

Feddersen, F., and J. H. Trowbridge (2005), The effect of wave breaking on surf-zone turbulence and alongshore currents: A modeling study, *J. Phys. Oceanogr.*, *35*(11), 2187–2203.

Feddersen, F., J. H. Trowbridge, and A. J. Williams (2007), Vertical structure of dissipation in the nearshore, *J. Phys. Oceanogr.*, *37*(7), 1764–1777.

Garcez Faria, A. F., E. B. Thornton, T. C. Lippmann, and T. P. Stanton (2000), Undertow over a barred beach, *J. Geophys. Res.*, *105*(C7), 16,999–17,010.

George, R., R. E. Flick, and R. T. Guza (1994), Observations of turbulence in the surf zone, *J. Geophys. Res.*, *99*(C1), 801–810.

Govender, K., G. P. Mocke, and M. J. Alport (2002), Video-imaged surf zone wave and roller structures and flow fields, *J. Geophys. Res.*, *107*(C7), 9-1–9-12.

Govender, K., H. Michallet, and M. J. Alport (2011), DCIV measurements of flow fields and turbulence in waves breaking over a bar, *Eur. J. Mech. B-Fluids*, *30*(6), 616–623.

Grasso, F., B. Castelle, and B. G. Ruessink (2012), Turbulence dissipation under breaking waves and bores in a natural surf zone, *Cont. Shelf Res.*, *43*, 133–141.

Huang, Z. C., S. C. Hsiao, H. H. Hwung, and K. A. Chang (2009), Turbulence and energy dissipations of surf-zone spilling breakers, *Coastal Eng.*, *56*(7), 733–746.

Hughes, S. (1993), *Physical Models and Laboratory Techniques in Coastal Engineering, Adv. Ser. on Ocean Eng.*, vol. 7, 571 pp., World Sci., Singapore.

Kimmoun, O., and H. Branger (2007), A particle image velocimetry investigation on laboratory surf-zone breaking waves over a sloping beach, *J. Fluid Mech.*, *588*, 353–397.

Melville, W. K., F. Veron, and C. J. White (2002), The velocity field under breaking waves: Coherent structures and turbulence, *J. Fluid Mech.*, *454*, 203–233.

Mori, N., T. Surzuki, and S. Kakuno (2007), Noise of acoustic doppler velocimeter data in bubbly flow, *J. Eng. Mech.*, *133*(1), 122–125.

Nadaoka, K., M. Hino, and Y. Koyano (1989), Structure of the turbulent-flow field under breaking waves in the surf zone, *J. Fluid Mech.*, *204*, 359–387.

Okayasu, A., T. Shibayama, and N. Mimura (1986), Velocity field under plunging waves, in *Proceedings of the 20th International Conference on Coastal Engineering, Taipei, Taiwan*, edited by B. L. Edge, pp. 660–674, Am. Soc. Civ. Eng., Reston, Va.

Peregrine, H. (1983), Breaking waves on beaches, *Annu. Rev. Fluid Mech.*, *15*, 149–178.

Petti, M., and S. Longo (2001), Turbulence experiments in the swash zone, *Coastal Eng.*, *43*, 1–24.

Raubenheimer, B., S. Elgar, and R. T. Guza (2004), Observations of swash zone velocities: A note on friction coefficients, *J. Geophys. Res.*, *109*, C01027, doi:10.1029/2003JC001877.

Ribberink, J. S., D. A. van der A, J. van der Zanden, T. O'Donoghue, D. Hurther, I. Cáceres, and P. Thorne (2014), SANDT-PRO: Sediment transport measurements under irregular and breaking waves, in *Coastal Engineering Proceedings*, vol. 34, edited by P. J. Lynett, pp. 1–14, ASCE/COPRI Coastal Eng. Res. Counc.

Ruessink, B. G. (2010), Observations of turbulence within a natural surf zone, *J. Phys. Oceanogr.*, *40*(12), 2696–2712.

Sancho, F., et al. (2002), Wave hydrodynamics over a barred beach, in *Proceedings of the Fourth International Symposium on Ocean Wave Measurement and Analysis*, edited by B. L. Edge and J. M. Hemsley, pp. 1170–1179, Am. Soc. Civ. Eng., Reston, Va. [Available at http://dx.doi.org/10.1061/9780784406045.]

Scott, C. P., D. T. Cox, T. B. Maddux, and J. W. Long (2005), Large-scale laboratory observations of turbulence on a fixed barred beach, *Measur. Sci. Technol.*, *16*(10), 1903–1912.

Shin, S., and D. Cox (2006), Laboratory observations of inner surf and swash-zone hydrodynamics on a steep slope, *Cont. Shelf Res.*, *26*(5), 561–573.

Smith, E., and N. Kraus (1991), Laboratory study of wave-breaking over fixed bars and artificial reefs, *J. Waterway, Port, Coastal Ocean Eng*, *117*(4), 307–325.

Sou, I. M., E. A. Cowen, and P. L.-F. Liu (2010), Evolution of the turbulence structure in the surf and swash zones, *J. Fluid Mech.*, *644*, 193–216.

Stansby, P. K., and T. Feng (2005), Kinematics and depth-integrated terms in surf zone waves from laboratory measurement, *J. Fluid Mech.*, *529*, 279–310.

Stive, M. J. F. (1985), A scale comparison of waves breaking on a beach, *Coastal Eng.*, *9*, 151–158.

Sumer, B. M., H. A. A. Guner, N. M. Hansen, D. R. Fuhrman, and J. Fredsøe (2013), Laboratory observations of flow and sediment transport induced by plunging regular waves, *J. Geophys. Res.*, *118*, 6161–6182, doi:10.1002/2013JC009324.

Svendsen, I. A. (1984), Wave heights and set-up in a surf zone, *Coastal Eng.*, *8*(4), 303–329.

Svendsen, I. A. (1987), Analysis of surf zone turbulence, *J. Geophys. Res.*, *92*(C5), 5115–5124.

Tennekes, H., and J. L. Lumley (1972), *A First Course in Turbulence*, MIT Press, Cambridge, Mass.

Thornton, E. B. (1979), Energetics of breaking waves within the surf zone, *J. Geophys. Res.*, *84*(C8), 4931–4938.

Ting, F. C. K., and J. T. Kirby (1994), Observation of undertow and turbulence in a laboratory surf zone, *Coastal Eng.*, *24*, 51–80.

Ting, F. C. K., and J. T. Kirby (1995), Dynamics of surf-zone turbulence in a strong plunging breaker, *Coastal Eng.*, *24*, 177–204.

Ting, F. C. K., and J. T. Kirby (1996), Dynamics of surf-zone turbulence in a spilling breaker, *Coastal Eng.*, *27*, 131–160.

Ting, F. C. K., and J. R. Nelson (2011), Laboratory measurements of large-scale near-bed turbulent flow structures under spilling regular waves, *Coastal Eng.*, *58*(2), 151–172.

Townsend, A. (1976), *The Structure of Turbulent Shear Flow*, 429 pp., Cambridge Univ. Press, Cambridge, U. K.

Trowbridge, J., and S. Elgar (2001), Turbulence measurements in the surf zone, *J. Phys. Oceanogr.*, *31*(8), 2403–2417.

van der Zanden, J. (2016), Sand transport processes in the surf and swash zones, PhD thesis, Univ. of Twente, Netherlands, doi:10.3990/1.9789036542456.

van der Zanden, J., D. A. van der A, D. Hurther, I. Cáceres, T. O'Donoghue, and J. S. Ribberink (2016), Near-bed hydrodynamics and turbulence below a full-scale plunging breaking wave over a mobile barred bed profile, *J. Geophys. Res. Oceans*, *121*, 6482–6506, doi:10.1002/2016JC011909.

Van Rijn, L. C., J. Ribberink, J. J. van der Werf, and D.-J. R. Walstra (2013), Coastal sediment dynamics: Recent advances and future research needs, *J. Hydraul. Res.*, *51*(5), 475–493.

Yoon, H. D., and D. T. Cox (2010), Large-scale laboratory observations of wave breaking turbulence over an evolving beach, *J. Geophys. Res.*, *115*, C10007, doi:10.1029/2009JC005748.